

Joint inversion for three-dimensional S velocity mantle structure along the Tethyan margin

Sung-Joon Chang,¹ Suzan van der Lee,¹ Megan P. Flanagan,² Heather Bedle,^{1,3} Federica Marone,^{4,5} Eric M. Matzel,² Michael E. Pasyanos,² Arthur J. Rodgers,² Barbara Romanowicz,⁴ and Christian Schmid^{6,7}

Received 1 January 2010; revised 17 March 2010; accepted 13 April 2010; published 21 August 2010.

[1] We construct a new three-dimensional S velocity model and Moho map by jointly inverting regional S and Rayleigh waveform fits, teleseismic S and SKS arrival times, fundamental mode Rayleigh wave group velocities, and independent Moho depth estimates for the region that extends from the mid-Atlantic ridge through northern Africa, southern Europe, and western Asia. The joint inversion benefits from both better resolution and wider data coverage than when using only individual data sets. Resolution tests confirm that the joint inversion yields good resolution ranging from the Moho to a depth of 1400 km. The complementary and overlapping nature of the different data sets' resolving power has reduced disparities in resolving power that exist for individual data sets, for example between resolving power for crustal and lower-mantle structure. This increases the utility of the new tomographic model for explaining and predicting a variety of observations and dynamics. The new model derived from the joint inversion assembles a large number of mantle structures known from a wide variety of previous studies into one model and in some cases reconciles different local studies that previously seemed contradictory. Finally, the model shows that shallow low-velocity anomalies beneath the Pannonian basin and the Iranian plateau are connected to similar anomalies in the transition zone, the latter possibly related to a deep dehydration process in the subducted lithosphere of the Neo-Tethys Ocean. The model shows the Hellenic slab penetrating the lower mantle, the Calabrian slab extending flatly in the transition zone, and discontinuous slabs beneath the Apennines and the Zagros belt.

Citation: Chang, S.-J., S. van der Lee, M. P. Flanagan, H. Bedle, F. Marone, E. M. Matzel, M. E. Pasyanos, A. J. Rodgers, B. Romanowicz, and C. Schmid (2010), Joint inversion for three-dimensional S velocity mantle structure along the Tethyan margin, *J. Geophys. Res.*, 115, B08309, doi:10.1029/2009JB007204.

1. Introduction

[2] The Tethyan margin extends from the westernmost Mediterranean Sea and North Atlantic Ocean eastward to the Himalayas. This region has complex tectonic structure primarily because of the convergence of the Eurasian plate with the Africa-Arabian and Indian plates that accompanied

the Mesozoic and Cenozoic subduction of the vast Tethys Oceans. In between the predominantly collisional tectonic features are a number of extensional basins, formed in back-arc settings. Overall, the Tethyan margin displays strong lateral variation and high-resolution three-dimensional (3-D) velocity structure is needed to explain and predict a range of observations and dynamics.

[3] The 3-D S velocity structure beneath all or parts of this region has been imaged with seismic tomography [e.g., Koulakov *et al.*, 2009; Marone *et al.*, 2004; Pasyanos, 2005]. These authors usually adopted arrival-time data or surface wave data, but each of these data sets has limitations. Arrival-time data offers excellent lateral resolution in regions of high seismicity or station density but have little resolving power beneath other regions. In addition, teleseismic arrival-time data have limited vertical resolution in the shallow mantle because the associated body wave ray-paths impinge steeply beneath the stations. On the other hand, surface waves provide critical information for aseismic regions with few stations because they traverse surface layers horizontally. However, regional S body waves and

¹Department of Earth and Planetary Sciences, Northwestern University, Evanston, Illinois, USA.

²Lawrence Livermore National Laboratory, Livermore, California, USA.

³Now at Chevron North America Exploration and Production Company, Gulf of Mexico SBU, Covington, Louisiana, USA.

⁴Berkeley Seismological Lab., University of California, Berkeley, California, USA.

⁵Now at Swiss Light Source, Paul Scherrer Institut, Villigen, Switzerland.

⁶ETH Zurich, Zurich, Switzerland.

⁷Now at Schweizerische Mobiliar Versicherungsgesellschaft, Bern, Switzerland.

as well as spreading ridges like the mid-Atlantic ridge, the Red Sea, and the Gulf of Aden. A number of hot spots, particularly in northern Africa, have been associated with localized deep low-velocity anomalies [e.g., *Crough*, 1979; *Sleep*, 1990].

[9] The Arabian plate consists of the Arabian shield and the Arabian platform, formed in the late Proterozoic, and the Arabian platform is covered by Phanerozoic strata. Possibly because of increase of regional buoyancy related to rifting along the Red Sea since the Miocene [*Almond*, 1986; *Bohannon et al.*, 1989], the Arabian shield is relatively elevated compared with the Arabian platform [*Daradich et al.*, 2003]. The Arabian shield also bears evidence of Neogene and Quaternary volcanism on its western and northern margin [*Camp and Roobol*, 1992].

[10] During the Eocene, the Indian plate collided with the Eurasian plate after relatively fast northward movement. This collision resulted in the generation of high-altitude regions like the Hindu Kush and the Himalayas at the eastern edge of our study region.

[11] More detailed overviews for the evolution of the Tethyan margin are given by *Dercourt et al.* [1986], *Dewey et al.* [1989], *Stampfli and Borel* [2002], and references therein.

1.2. Previous S Velocity Mantle Structure Studies

[12] A recent study by *Koulakov et al.* [2009] utilized ISC arrival time data to estimate S velocity mantle structure beneath Europe down to 700 km depth. Their model shows good lateral resolution, but loses resolution in aseismic regions with few stations and the vertical resolution in the shallow mantle is much reduced from that in the deep upper mantle.

[13] Inversions of surface wave phase/group velocity data have been conducted for the estimation of S velocity in the shallow upper mantle beneath the larger Mediterranean region [*Pasyanos et al.*, 2001; *Pasyanos and Walter*, 2002; *Pasyanos*, 2005; *Peter et al.*, 2008; *Ritzwoller and Levshin*, 1998; *Schivardi and Morelli*, 2009; *Villaseñor et al.*, 2001]. For the Africa region, *Ritsema and van Heijst* [2000] derived an S velocity model for the shallow mantle with fundamental mode Rayleigh wave phase velocity data for periods ranging from 40 to 200 s. *Yang et al.* [2007] performed ambient noise tomography with Rayleigh wave dispersion curves with 8 to 50 s period to assess crust and uppermost mantle structure. All of these surface wave studies show the less lateral resolution than the seismic body wave studies in well-covered regions.

[14] S velocity models can be obtained by fitting regional S - and surface wave trains. *Zielhuis and Nolet* [1994] modeled the upper mantle S velocity of Europe and part of the Mediterranean region, using the partitioned waveform inversion (PWI) [*Nolet*, 1990]. *Maggi and Priestley* [2005] and *Marone et al.* [2004] applied PWI to the Anatolian-Iranian plateau and the Mediterranean region, respectively. S velocity models by *Marone et al.* [2004] and *Zielhuis and Nolet* [1994] have vertical resolution down to around 600 km depth, deeper than aforementioned results from surface wave tomography because of the use of higher modes and regional body waves.

[15] *Schmid et al.* [2008] combined regional S - and surface waveform fits, teleseismic S arrival times, and inde-

pendent Moho constraints to obtain an S velocity model for the Mediterranean region. We expand on this study by extending the study region eastward to eastern India and by also incorporating Rayleigh wave group velocity data. We expect that this new combination of data sets provides resolving power down to 1400 km that is superior to the resolving power of any individual data set.

2. Model Parameterization

[16] We use a spherical shell of grid points to support the S velocity distribution at each of 32 depths, as well as one shell to support the Moho. Our spherical shells of grid points reach 1930 km down into the mantle and are located at 0, 5, 10, 20, 30, 45, 60, 80, 100, 130, 160, 200, 240, 280, 320, 360, 410, 470, 530, 590, 660, 730, 810, 900, 1000, 1110, 1230, 1360, 1500, 1640, 1780, and 1930 km. At each depth, these grid points are derived through triangular tessellation of a sphere, an approach first used in geoscience in finite element modeling by *Baumgardner and Frederickson* [1985]. The 3-D S velocity structure is defined through trilinear interpolation of S velocity anomaly values at grid points. The laterally varying Moho depth is analogously defined, using bilinear interpolation. The center of our grid is located at 35N and 22.5°E and extends 70° in all directions from this point. Each shell contains 16,541 grid points spaced roughly 100 km apart on the surface. Including the Moho we have a total of 545,853 grid points. However, only about 63% (343,841) are sampled by our data.

[17] Our S velocity anomalies are relative to the one-dimensional reference S velocity model “MEAN” [*Marone et al.*, 2004], which is a modified version of *iasp91* [*Kennett and Engdahl*, 1991] to reflect the average characteristics of a tectonically active mix of oceanic and continental regions.

3. Method

[18] We arrange the S velocity perturbations ($\Delta\beta$) at grid nodes of a 3-D grid and Moho depth perturbations (Δh) at grid nodes on a two dimensional grid in a model vector \mathbf{m} . This model vector also has elements that represent corrections for hypocenter location and origin time (Δx_e and Δe) for each event for which we collected teleseismic travel times. Differences between observed data of various types and data predicted by the reference model are arranged in data vector \mathbf{d} . Partial derivatives of the various data types with respect to the model parameters constitute the Fréchet (sensitivity) kernel matrix \mathbf{G} . These three components form a set of linear equations, typical in seismic tomography:

$$\mathbf{Gm} = \mathbf{d}. \quad (1)$$

We find a tomographic model \mathbf{m} by solving this large, sparse, and mixed-determined system of equations using a regularized version of the iterative conjugate-gradient algorithm LSQR [*Paige and Saunders*, 1982a, 1982b]. The contributions to the sensitivity kernel matrix \mathbf{G} and data vector \mathbf{d} from different data types are calculated as follows.

[19] To incorporate regional S and Rayleigh waveform fits in the inversion, we utilized PWI [*Nolet*, 1990; *van der Lee and Nolet*, 1997]. First, waveforms were fitted non-linearly using a damped Newton’s method for the best

one-dimensional model for the corresponding great circle wave path. Synthetic seismograms to be compared with observed ones were constructed through summing surface wave mode branches. The misfit function is defined as

$$F(\gamma) = \int \varpi(t) [\mathbf{R}d(t) - \mathbf{R}s(t, \gamma)]^2 dt \quad (2)$$

where $d(t)$ and $s(t, \gamma)$ are observed and synthetic seismograms, respectively. Coefficients in γ represent a linear combination of basis functions that reflects the best, path-averaged one-dimensional velocity model for the wave path under consideration. Weighting function $\varpi(t)$ serves to mitigate, for example, the dominance of high-amplitude surface waves over lower-amplitude S waves and \mathbf{R} represents a filtering and windowing operator. The principal components γ of the best one-dimensional model form linear equations for use in the joint inversion. Extensive details of PWI are given by *Nolet* [1990] and *van der Lee and Nolet* [1997]. The linear equation reads as follows:

$$\gamma_i = \sum_j A_{ij}^{rw} \Delta\beta_j + \sum_m A_{im}^{rw} \Delta h_m \quad (3)$$

where A_{ij}^{rw} , A_{im}^{rw} are sensitivity kernel matrices that incorporate the depth dependence of the basis functions corresponding to each element of γ , the lateral averaging along the great circle path between the earthquake and recording seismic stations, as well as the tri- and bi-linear interpolation scheme that defines our 3-D S velocity model $\Delta\beta$ and two-dimensional Moho depth perturbations Δh , respectively.

[20] We also collected and incorporate in the inversion absolute and relative teleseismic arrival times. Predicted arrival time delays are approximated as follows, using Fermat's principle and ignoring third- and higher-order terms,

$$\delta t \approx - \int_{L_0} \frac{1}{\beta_0} \frac{\delta\beta}{\beta_0} dl \quad (4)$$

where δt is the delay time accumulated along the unperturbed raypath L_0 . S velocity perturbations $\delta\beta$ are relative to velocity β_0 in the reference model. With additional consideration of the effect of Moho depth and event mislocation on delay times, equation (4) can be discretized as follows:

$$\Delta t_i = \sum_j A_{ij}^{ta} \Delta\beta_j + \sum_m A_{im}^{ta} \Delta h_m + A_e^{ta} \Delta x_e + A_o^{ta} \Delta e \quad (5)$$

where sensitivity kernel matrix elements A_{ij}^{ta} and A_{im}^{ta} indicate partial derivatives of the arrival time with respect to S velocity perturbation $\Delta\beta$ and the Moho depth perturbation Δh , respectively. Matrix elements A_e^{ta} and A_o^{ta} include partial derivatives of arrival time with respect to location vector and to origin time of each event (Δx_e and Δe), respectively. Rays are traced with the shooting method according to *VanDecar* [1991]. We do not include station terms in equation (5), because shallow structure represented by station terms is included in the sensitivity of Rayleigh wave group velocity and regional waveform fit

data. Arrival times are corrected for topography and Earth's ellipticity prior to inversion.

[21] We incorporate new and previously measured Rayleigh wave group velocities in the inversion. We calculate partial derivatives of Rayleigh wave group velocity with respect to S velocity perturbation following *Rodi et al.* [1975]. The group velocity perturbation is represented as follows:

$$\Delta U_i = \sum_j A_{ij}^U \Delta\beta_j + \sum_m A_{im}^U \Delta h_m \quad (6)$$

where matrix elements A_{ij}^U and A_{im}^U indicate partial derivatives of group velocity with respect to S velocity perturbation and the Moho perturbation, respectively. The matrix element A_{im}^U is numerically calculated from a first-order approximation, $\partial U/\partial h \approx \Delta U/\Delta h$ with $\Delta h = 1$ km. Because the group velocities are measured at up to 21 periods between 7 and 100 s per seismogram, the ΔU measurements are significantly redundant. To reduce this redundancy and increase the validity and efficiency of the least squares inversion, we performed singular value decomposition [*Dongarra et al.*, 1979] of (6) for each seismogram and discarded constraints with singular values less than 10% of the maximum singular value.

[22] To avoid mapping shallow velocity perturbations into Moho depth variations and vice versa, we introduce additional equations from independent studies that constrain Moho depth. The linear equations are given as

$$\Delta H_i = \sum_m A_{im}^{ic} \Delta h_m = d^{ic} \quad (7)$$

where A_{im}^{ic} reflects coefficients that project the measurement location onto the two-dimensional Moho grid and ΔH_i is the difference between observed Moho depth and Moho depth in the reference model. These point constraints are obtained from published analyses of receiver functions, gravity measurements, refraction and reflection surveys, and are further described in section 4.

[23] Both group velocity data and regional waveform data are more distinctly sensitive to Moho depth than the teleseismic arrivals. Partial derivatives of regional waveforms and fundamental mode group velocities to S velocity are calculated for each seismogram with one of several different one-dimensional reference models. Each one-dimensional model reflects an average Moho depth and average ocean depth that are appropriate for the wave path under consideration.

[24] Equations (3), (5), (6), and (7) are combined in matrix form as

$$\begin{bmatrix} w_{ia} \mathbf{A}^{ta} & w_{im} \mathbf{A}_m^{ta} & w_{ie} \mathbf{A}_e^{ta} & w_{io} \mathbf{A}_o^{ta} \\ w_{rw} \mathbf{A}^{rw} & w_{rm} \mathbf{A}_m^{rw} & 0 & 0 \\ w_U \mathbf{A}^U & w_{Um} \mathbf{A}_m^U & 0 & 0 \\ 0 & w_{ic} \mathbf{A}_m^{ic} & 0 & 0 \end{bmatrix} \begin{bmatrix} \Delta\beta \\ \Delta h \\ \Delta x_e \\ \Delta e \end{bmatrix} = \begin{bmatrix} w_{ia} d^{ta} \\ w_{rw} d^{rw} \\ w_U d^U \\ w_{ic} d^{ic} \end{bmatrix}. \quad (8)$$

We scaled each datum with the inverse of the corresponding measurement error (uncertainty) to weight each

datum according to its quality. The values w_{ta} , w_{rw} , w_U , and w_{ic} are additional weights for data sets of teleseismic arrivals, regional waveform fits, Rayleigh wave group velocities, and independent Moho constraints, respectively, to ensure that each of the data sets can be fitted to the acceptable level for that data set by accounting for data quantity.

[25] Because equation (8) is partly underdetermined, we have to add regularization constraints to the system of equations such as damping and flattening. The regularization operator is given by

$$\mathbf{R} = \begin{bmatrix} w_1 \mathbf{I} \\ w_2 \mathbf{F}_h \\ w_3 \mathbf{F}_v \end{bmatrix} \quad (9)$$

where \mathbf{I} is the identity matrix; \mathbf{F}_h and \mathbf{F}_v are horizontal and vertical flattening operators, respectively. The values of w_i ($i = 1, 2, 3$) are weights for each operator. The damping operator plays a role to suppress the effects of data outliers, and the flattening operators keep model parameters from rapid nonphysical variations. Flattening operators are differentials between two lateral or vertical contiguous grid points [Constable *et al.*, 1987; VanDecar, 1991]. Similar regularization is applied to Moho depth perturbations. If we incorporate equation (9) into equation (8), the equation is written as

$$\begin{bmatrix} w_{ta} \mathbf{A}^{ta} & w_{ta} \mathbf{A}_m^{ta} & w_{ta} \mathbf{A}_e^{ta} & w_{ta} \mathbf{A}_o^{ta} \\ w_{rw} \mathbf{A}^{rw} & w_{rw} \mathbf{A}_m^{rw} & 0 & 0 \\ w_U \mathbf{A}^U & w_U \mathbf{A}_m^U & 0 & 0 \\ 0 & w_{ic} \mathbf{A}_m^{ic} & 0 & 0 \\ w_1 \mathbf{I} & w_1 \mathbf{I} & 0 & 0 \\ w_2 \mathbf{F}_h & w_2 \mathbf{F}_h & 0 & 0 \\ w_3 \mathbf{F}_v & 0 & 0 & 0 \end{bmatrix} \begin{bmatrix} \Delta\beta \\ \Delta h \\ \Delta x_e \\ \Delta e \end{bmatrix} = \begin{bmatrix} w_{ta} d^{ta} \\ w_{rw} d^{rw} \\ w_U d^U \\ w_{ic} d^{ic} \\ 0 \\ 0 \\ 0 \end{bmatrix}, \quad (10)$$

which is the final matrix equation we solve for S velocity and Moho perturbations from the reference model.

4. Data

[26] We obtained seismic data from a combination of permanent and temporary broadband seismic networks spread throughout the study region: Geofon [Hanka and Kind, 1994], GeoScope [Romanowicz *et al.*, 1984], GRF [Harjes and Seidl, 1978], GRSN [Hanka, 1990], IRIS-IDA [Agnew *et al.*, 1986], IRIS-USGS [Peterson and Hutt, 1989], ISN [Gitterman *et al.*, 1998], MedNet [Boschi *et*

al., 1991], MIDSEA [van der Lee *et al.*, 2001], NARS [Paulssen, 1992], PASSCAL, Swiss National Network [Baer, 1990], Saudi Arabian National Digital Seismic Network [Al-Amri and Al-Amri, 1999], Università di Trieste, RéNaSS, TGRS, Universität Stuttgart, Universidad de Barcelona, Universidad Autónoma de Madrid, Institute Andaluz, Czech National Seismological Network, GI_Budapest and Blacknest.

[27] In addition to using 1136 regional waveform fits of Marone *et al.* [2004] for Europe and the Mediterranean Sea, we have fitted around 4500 new waveforms that sample the Middle East, Afghanistan, Pakistan, northern and eastern Africa, the Red Sea, and part of the East European platform. The great circle wave propagation paths for all of these seismograms with locations of events and stations are shown in Figure 2. We utilized events with magnitude larger than 4.0 and seismograms with epicentral distance from 5° to 50°. Events with magnitude smaller than 5.0 are used only at relatively short epicentral distances. For the comparison with observed waveforms, we calculated synthetic waveforms with the centroid moment tensors (CMT) from the Global CMT catalog [e.g., Dziewonski *et al.*, 1994] and hypocenters from Engdahl's reprocessed ISC database [Engdahl *et al.*, 1998; E. R. Engdahl, personal communication, 2007]. Although it is different for each waveform fit, the retained frequency content of observed waveforms and synthetics generally falls within the range of 0.006 and 0.1 Hz.

[28] We obtained S and SKS phase arrival time data from two different sources. Both arrival times are adjusted for topography and Earth's ellipticity before inversion. First, we used high quality relative arrival times of teleseismic S and SKS waves, which are measured with multichannel cross-correlation method (MCCC) of VanDecar and Crosson [1990] in Ethiopia, Arabia, and the Mediterranean region by Benoit *et al.* [2006], Park *et al.* [2007], and Schmid *et al.* [2004], respectively. Moreover, we measured additional relative delay times using seismograms from a PASSCAL experiment (Eastern Turkey Seismic Experiment), the Kyrgyz Seismic Telemetry Network (KNET), and the Kazakhstan Network (KZNET). The total number of S phase relative arrival times is over 5900, covering epicentral distances of 30° to 90° and the number of SKS phase arrival times is over 1400, covering distances of 87° to 140°. We estimate the uncertainty for each of these relative delay times at 0.5 s, which is used to weight the equations before they are joined with equations from other data types.

[29] Second, we obtained over 223,000 S phase arrival time data from the reprocessed ISC database [Engdahl *et al.*, 1998; E. R. Engdahl, personal communication, 2007] from 1964 to 2007. We extracted S phases from this database with a listed precision of 1 s or less if station and/or epicenter are located in the study region. The epicentral distance range is 20° to 80°. Because our regional waveform and group velocity data support the existence of Earth structure that can cause large teleseismic delay times, we do not systematically remove large residuals before inversion. However, because some large residuals are the results of mispicks and other systematic errors [Röhm *et al.*, 2000], this choice might hamper our ability to achieve a large variance reduction for this data set. To minimize the effect of true outliers we estimate the uncertainty for each of

Wave Paths for Waveform Fits

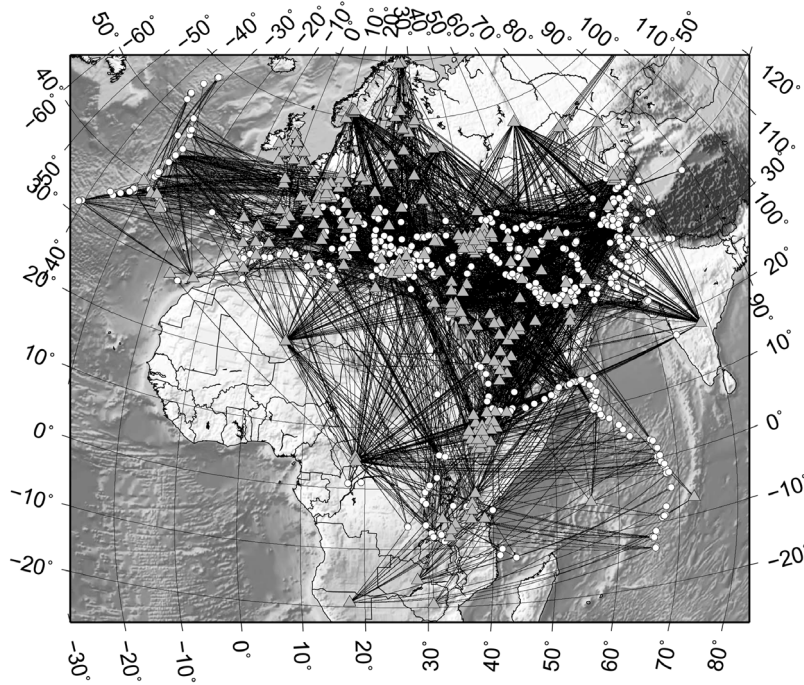


Figure 2. Great circle wave paths for waveform fits. Stations are illustrated as gray triangles and events as white circles.

Events and Stations for Teleseismic Arrival Times

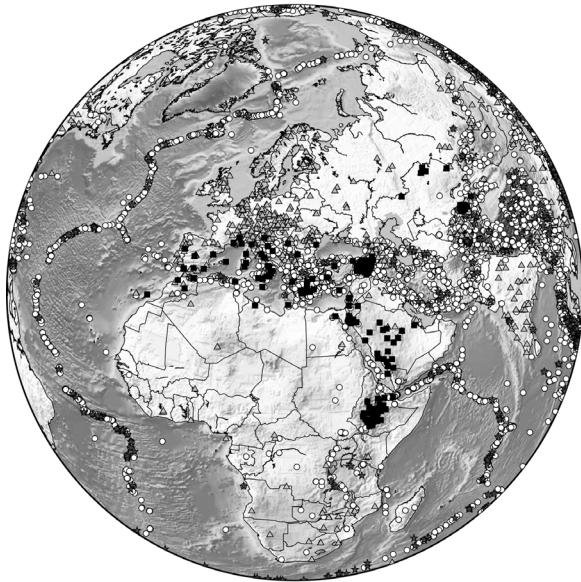


Figure 3. Events and stations used for teleseismic *S* and *SKS* arrival time estimation. Dark gray stars and black squares represent events and stations used for relative delay time estimation with MCCC, respectively. White circles and light gray triangles mean events and stations from the reprocessed ISC catalog, respectively.

these arrival-time picks relatively high at 3.0 s. This estimate effectively downweights this data set with respect to the smaller data set of relative arrival times from cross-correlation measurements discussed above. Figure 3 illustrates location of stations and events for each of the two types of arrival-time data.

[30] Figure 4 shows an example of teleseismic *S* and *SKS* wave paths in our data set that lie within half a degree from

Ray Paths for Teleseismic S and SKS Waves

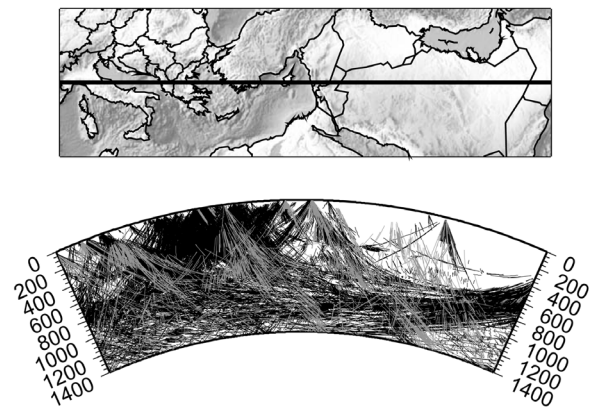


Figure 4. A cross section through the study region where segments of raypaths of teleseismic *S* and *SKS* waves within half a degree from the vertical plane are projected. Teleseismic wave paths from the ISC catalog and MCCC technique are indicated in black and gray lines, respectively.

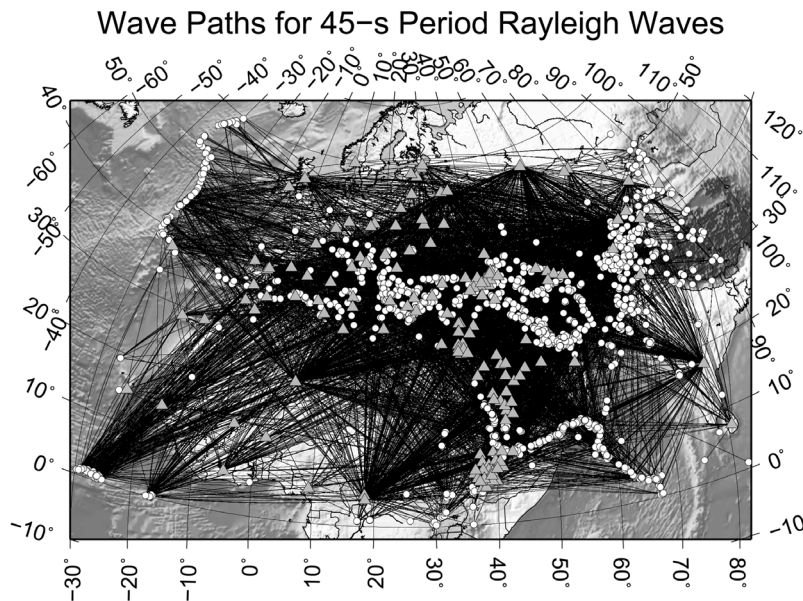


Figure 5. Great circle wave paths for 45 s period Rayleigh waves. Stations are illustrated as gray triangles and events as white circles.

the cross section. Although the top of the lower mantle and the transition zone are well covered by these data, large data gaps in the upper mantle beneath seismically inactive and sparsely instrumented regions such as Arabia, the eastern Mediterranean Sea, and the Algero-Provençal basin exist, illustrating the need to complement the teleseismic arrival time data with group velocity and regional waveform data, which are also sensitive to upper-mantle structure between earthquakes and seismic stations. Moreover, the lateral resolving power of teleseismic arrival time data from near-vertical raypaths in the uppermost mantle complements well the vertical resolving power of group velocities and waveform fits on account of their varying depth sensitivity with frequency and mode number.

[31] Fundamental mode Rayleigh wave group velocity dispersion curves were measured on vertical broadband displacement seismograms filtered by a narrow-band Gaussian filter over many periods [e.g., *Dziewonski et al.*, 1969; *Herrmann*, 1973; *Levshin et al.*, 1972]. Group velocities are estimated from the arrival time of the maximum amplitude in each envelope function for different period ranges of between 7 and 100 s. A detailed explanation for estimating dispersion measurements is given by *Pasyanos et al.* [2001]. Including new group velocity data from waveforms recorded at MIDSEA network, the number of total fundamental mode Rayleigh wave group velocity dispersion curves is expanded from that used by *Pasyanos et al.* [2001] and *Pasyanos* [2005] to 8861. Although fundamental mode group velocity data are sensitive to a relatively shallow part of the upper mantle, compared to regional waveform fits and teleseismic arrival times, their lateral path coverage is better than these other data sets, as shown in Figure 5.

[32] To further confine Moho depth, we include independent estimates of crustal thickness as point constraints in the joint inversion from a large number of published studies [*Al-Damegh et al.*, 2005; *Al-Lazki et al.*, 2002; *Julià and*

Mejia, 2004; *Kumar et al.*, 2002; *Li et al.*, 2003; *Marone et al.*, 2003; *Mooney et al.*, 2002; *Mohsen et al.*, 2005; *Paul et al.*, 2006; *Sandvol et al.*, 1998; *Sodoudi*, 2005; *Tkalčić et al.*, 2006; *Wilde-Piörko et al.*, 2005; *Zor et al.*, 2003]. We obtained over 4700 Moho depth constraints from these studies using receiver functions, gravity measurements, refraction, and reflection surveys. An extensive list of references for these constraints is provided by *Marone et al.* [2003]. For Moho depths from receiver function studies we use the uncertainty reported by these studies. Where uncertainties are not reported we estimate it to be 2 km. We estimate the uncertainty in Moho depths from gravity studies at 6 km. For Moho depths from refraction and reflection surveys we estimate the uncertainty at 4 km. The Moho depth constraints are mapped in Figure 6. In

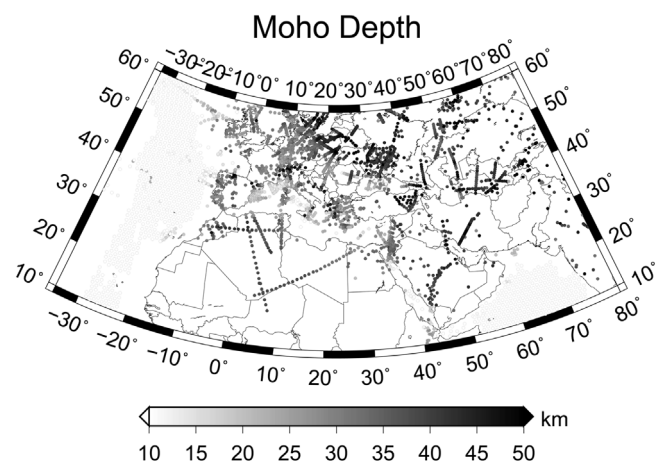


Figure 6. Map of the Moho depth distribution acquired from previous studies. Artificial point constraints of 10 km depth are put to the Atlantic Ocean and the Arabian Sea where measurements are absent.

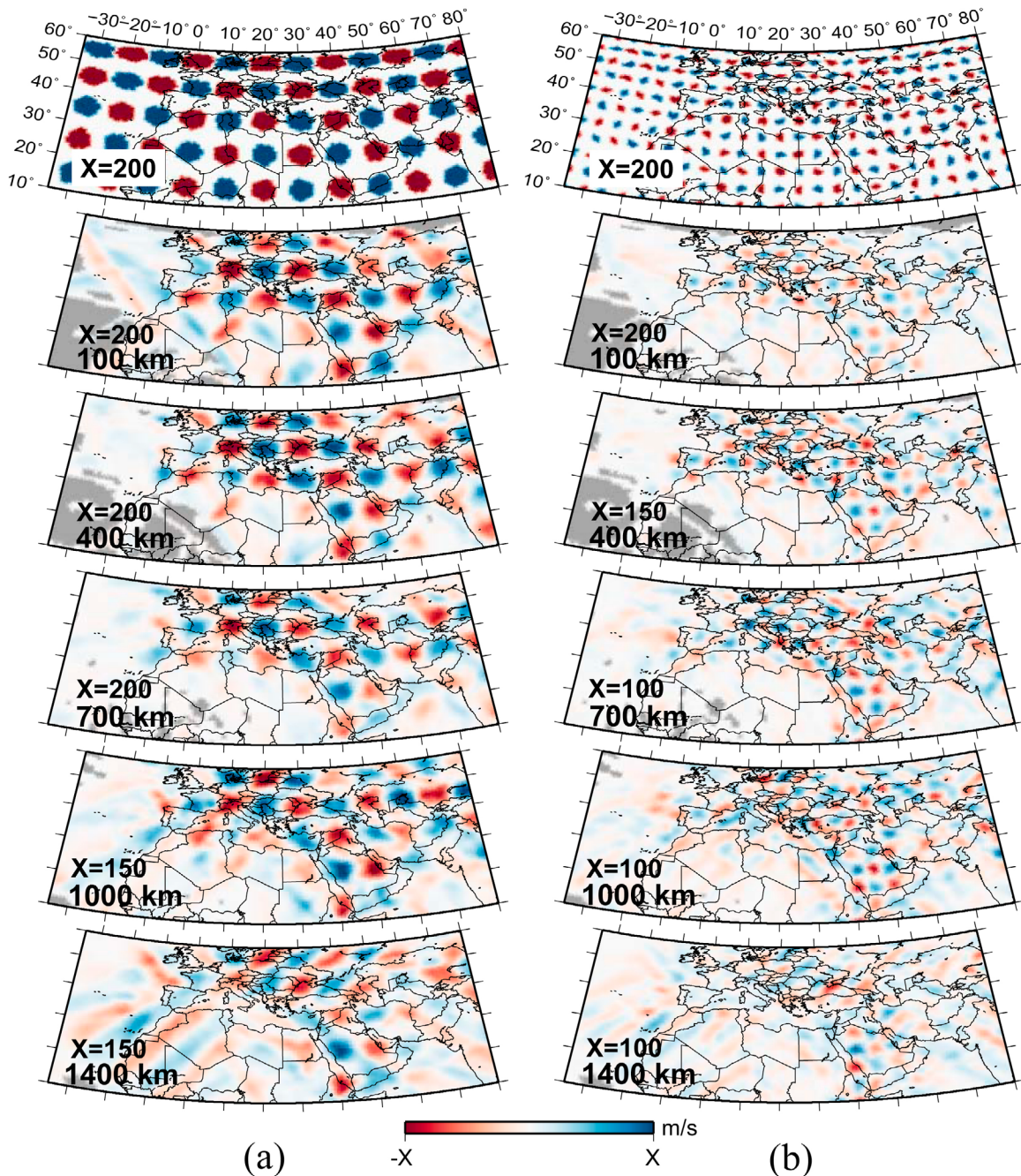


Figure 7. Resolution tests with noise contamination. The horizontal slices of S velocity perturbations with radii of (a) 3° and (b) 1° in the true model and joint inversion results at various depths are presented. Regions not covered by combined data sets are illustrated in gray.

oceans, where such measurements are absent, we create point constraints that encourage the Moho depth to be at a depth of 10 km with an error bound of 6 km. We set these artificial point constraints to only oceans where the Moho depth in CRUST2.0 [Bassin *et al.*, 2000] is shallower than 15 km depth.

5. Resolution Tests

[33] To assess the resolving power of our data we performed a variety of tests. For these tests we calculated

synthetic data vectors \mathbf{d}_S by multiplying test models with the sensitivity kernel matrices in equation (10). We add Gaussian random noise to \mathbf{d}_S with a standard deviation in proportion to the estimated uncertainty of our data. We then invert the resulting data vectors \mathbf{d}_S' to obtain solutions that would be identical to the test models in an ideal case of perfect resolution. Because our data cannot resolve Earth structure perfectly, these tests help indicate the extent to which our data *can* resolve Earth structure.

[34] Figure 7a illustrates joint inversion results in map view for a test model with anomalies of $\pm 200 \text{ m s}^{-1}$ that are

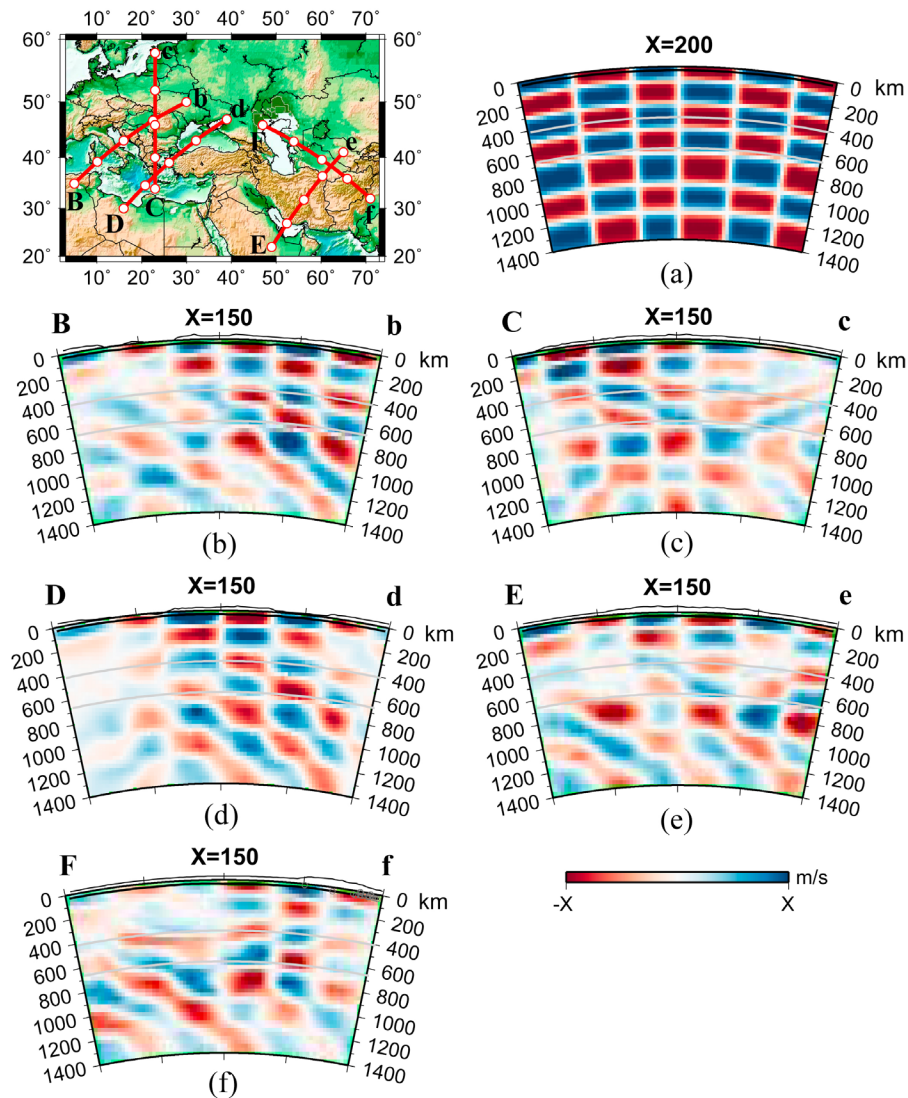


Figure 8. Resolution tests for vertical cross sections. Vertical profiles are presented for (a) the true model and beneath (b) the Apennines, (c) the Pannonian basin, (d) the Hellenic arc, (e) the Zagros belt, and (f) from the Caspian Sea to northern India. Moho depth and surface topography are shown in black solid lines. Topography is exaggerated 10 times. Light gray lines indicate 410 and 660 km discontinuities. Great circle paths corresponding to cross sections are indicated on the left-top map. White circles on the great circle paths correspond to ticks shown in the cross sections.

vertical cylinders, each with a radius of 3° . At 100 km depth, the joint inversion result recovered velocity anomalies very well beneath Europe, the Mediterranean Sea, and the Middle East. However, we have limited resolution beneath the Atlantic Ocean, the Arabian Sea, and West Africa due to poor data coverage. Anomalies continue to be well resolved with increasing depth throughout the upper mantle and the transition zone for most regions, albeit with a decrease in anomaly amplitude. In the lower mantle, the recovered amplitude decreases further and smearing effects are stronger. Nevertheless, velocity anomalies are relatively well recovered down to 1400 km for the Mediterranean region, eastern Europe, the Middle East, and central Asia. When we reduce the radii of the cylindrical anomalies to 1° , the decrease in recovered anomaly amplitude is, as expected, more severe (Figure 7b). However, anomalies down

to the uppermost lower mantle beneath Europe, the Mediterranean Sea, and the Middle East remain relatively well resolved. Beneath Arabia, anomalies are well resolved down to as deep as 1000 km.

[35] Figure 8 illustrates the resolving power of the joint data sets for vertical variations in velocity. We use a checkerboard test model (Figure 8a). The thickness of anomaly checkers of $\pm 200 \text{ m s}^{-1}$ is 100 km for the first layer, 200 km for the upper mantle and the transition zone, and 250 km for the lower mantle. Anomalies in the upper mantle and the transition zone are well resolved in most of the study region. Smearing effects are observed in the lower mantle but good resolution is obtained for some cross sections, for example, those in Figures 8c and 8e.

[36] We also used the three-dimensional global tomographic P velocity model of *Bijwaard et al.* [1998] as a test

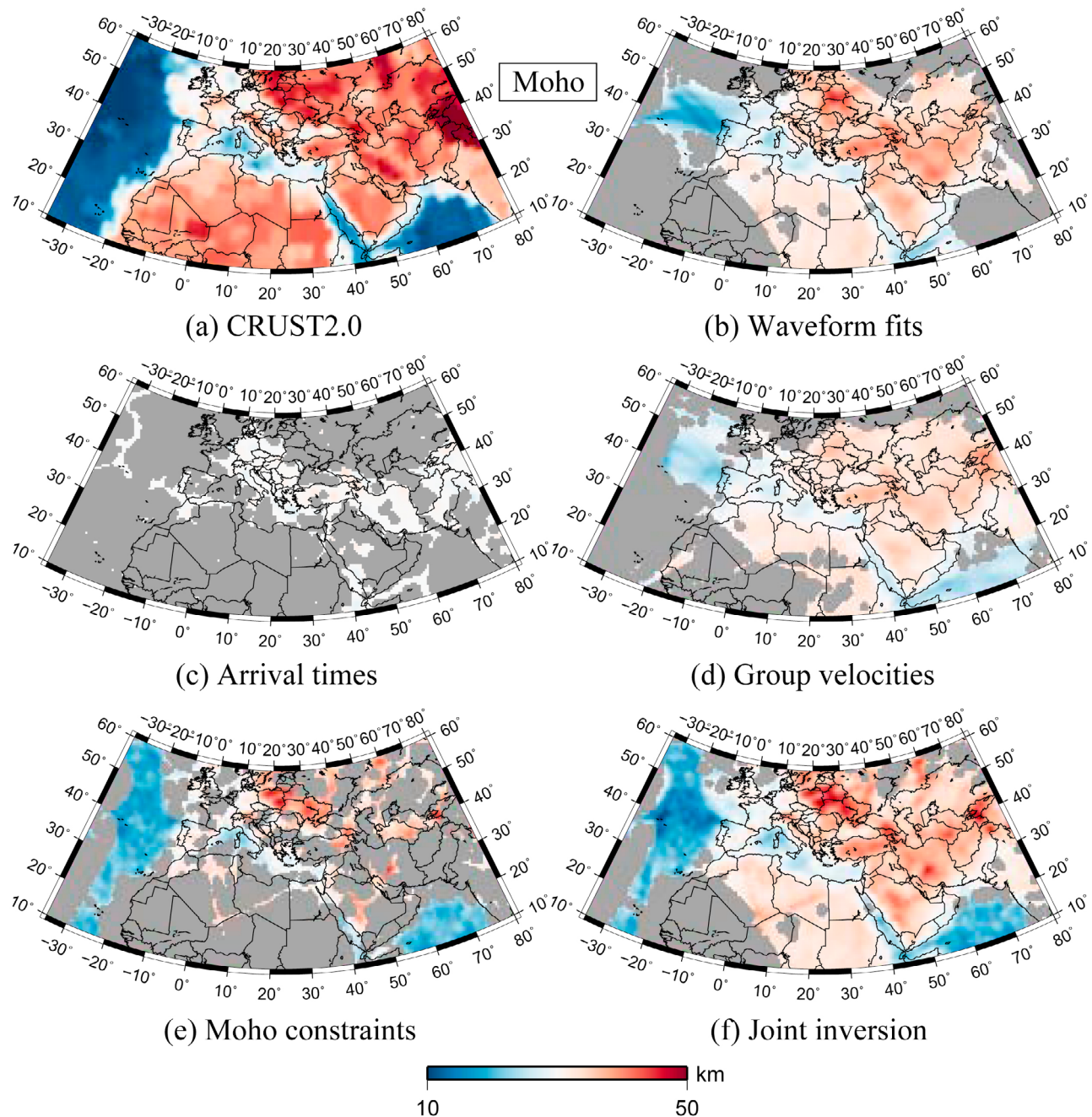


Figure 9. Resolution tests with noise contamination for Moho depth distributions. The Moho depth distributions (a) in the hypothetical model (CRUST2.0) and inversion results with contaminated synthetic data (b) of waveform fits, (c) of arrival times, (d) of group velocities, (e) of Moho constraints, and (f) of the combined data sets are presented. Regions not covered by data sets are illustrated in gray.

model. To convert their *P* velocity model to a testable *S* velocity model, we applied an arbitrary, though reasonable scaling. We call this test model BSES. We added CRUST2.0 (Bassin et al., 2000) to the BSES model to incorporate lateral variations in Moho depth. We followed the same process to make synthetic data sets as in the previous resolution tests. In order to investigate the difference in resolving power and data coverage of each data set, we performed stand-alone inversions with individual

data sets as well as a joint inversion with the combined data sets.

[37] The joint inversion and stand-alone inversion results for Moho variation are shown in Figure 9. Waveform fits and group velocity measurements have not only wide data coverage but also good resolving power for the Moho, although Moho variations recovered by the group velocity data are somewhat flattened. As expected, our arrival time data are virtually incapable of discriminating Moho depth

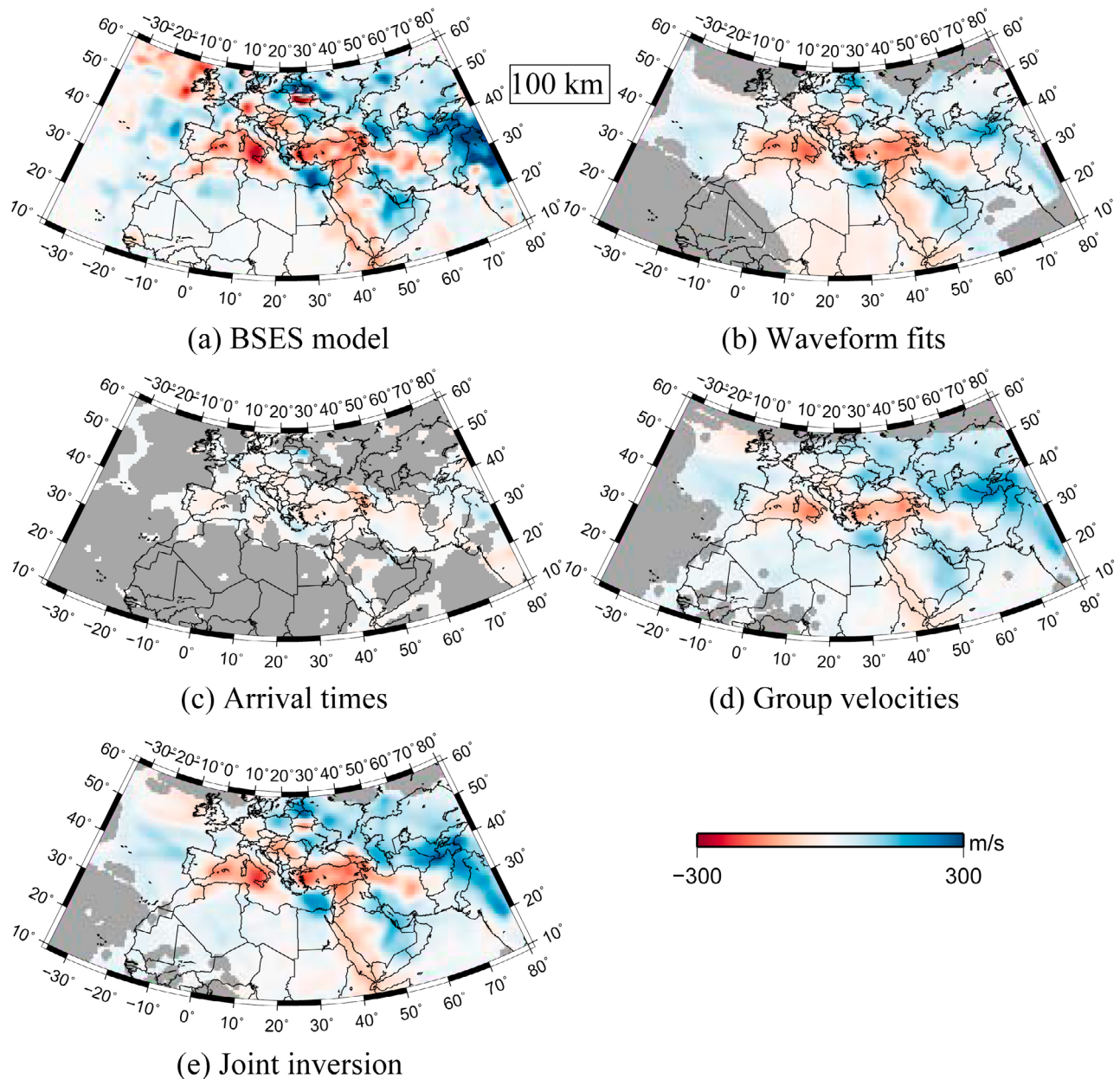


Figure 10. Resolution tests with noise contamination for S velocity perturbations at 100 km depth. The horizontal slices of S velocity perturbations (a) in the BSES model and inversion results with contaminated synthetic data (b) of waveform fits, (c) of arrival times, (d) of group velocities, and (e) of the combined data sets are presented. Regions not covered by data sets are illustrated in gray.

variations from velocity variations. The Moho depth from the joint inversion agrees significantly better with CRUST2.0 than results from the stand-alone inversions, especially for Europe, the Mediterranean Sea, and the Middle East. This is in part because of jointly inverting these different data sets and in part because of the additional inclusion of independent constraints on Moho depth (see section 3).

[38] Figures 10–13 are maps of inversion results at various depths with individual and combined data sets. Regional waveform fits and group velocity measurements have good resolving power around 100 km depth, while our arrival times have poor resolving power at this depth (Figure 10). At 400 km, the resolving power of fundamental mode group

velocities has vanished, but arrival times resolve structure much better (Figure 11) than at 100 km depth (Figure 10) because of better crisscrossing of the curved raypaths. At depths around 700 km (Figure 12), regional waveform fits lose resolving power, and teleseismic arrival times have excellent resolving power, dominating the joint inversion. At 1000 and 1400 km depth (Figure 13) only the teleseismic arrival times have resolving power. The joint inversion result agrees well with the BSES model, despite the presence of Gaussian random noise in our synthetic data sets. The resolving power of the joint inversion is better in all aspects than that of stand-alone inversions. However, some small anomalies remain smeared out and the damping and

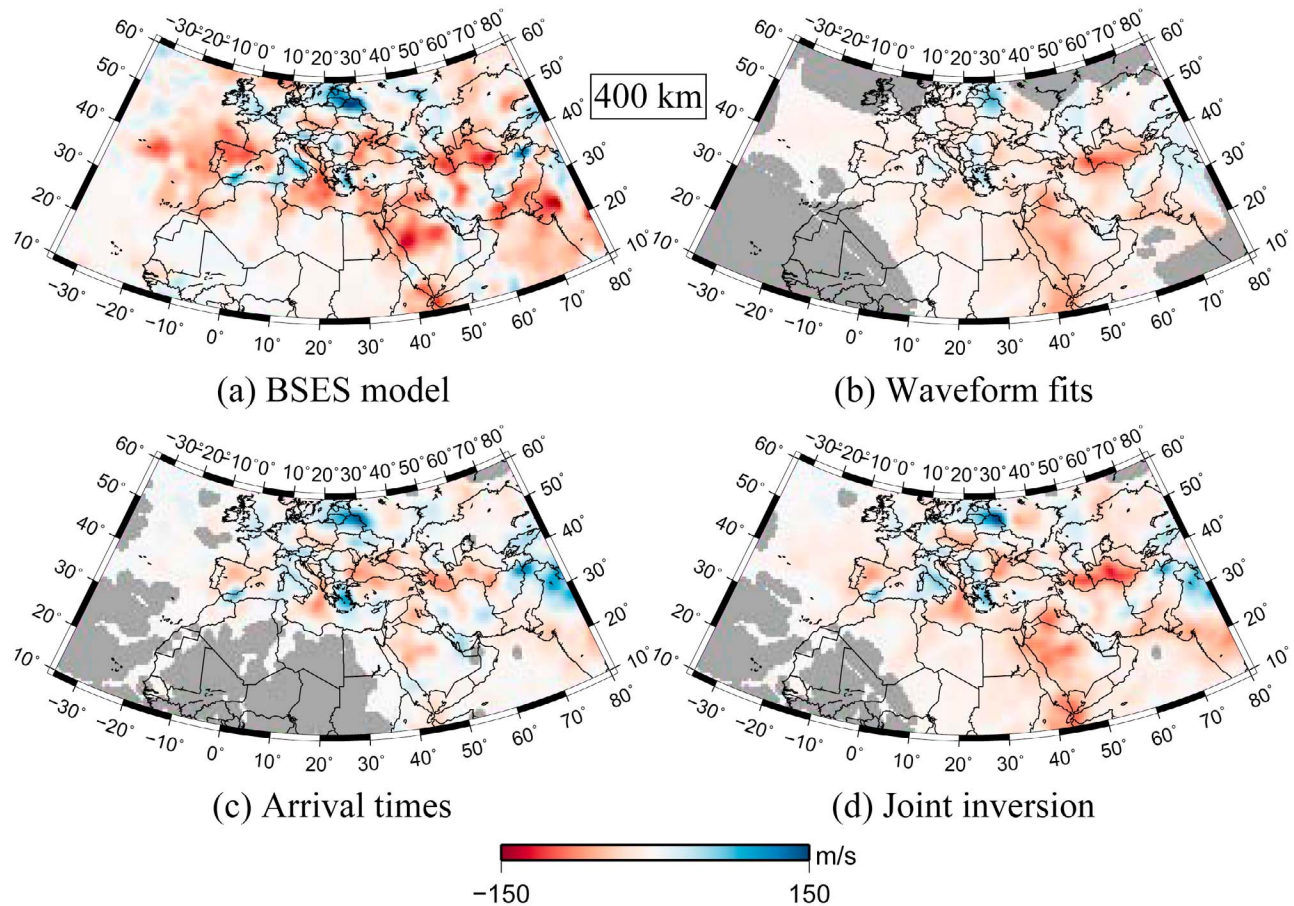


Figure 11. Resolution tests with noise contamination for S velocity perturbations at 400 km depth. The horizontal slices of S velocity perturbations (a) in the BSES model and inversion results with contaminated synthetic data (b) of waveform fits, (c) of arrival times, and (d) of the combined data sets are presented. Regions not covered by data sets are illustrated in gray.

flattening operators used in the regularized inversion continue to preferentially underestimate the amplitude of recovered anomalies.

[39] Figure 14 shows cross sections through the same set of models from the joint inversion and stand-alone inversions shown in Figures 9–13. Anomalies down to around 150 km depth can be detected with group velocities for periods from 7 to 100 s, but there is an artificial velocity inversion below this depth. Regional waveform fits have resolving power, which decreased with increasing depth, to as deep as 600 km. In contrast, teleseismic arrival times show their best resolving power for the lower mantle and the transition zone line. In general, the main features in the BSES model are well recovered in our joint inversion. We find that it is difficult to fully infer mantle structure in all three dimensions with only one kind of seismic data. Using various kinds of seismic data with different resolving power produces more complete and more accurate tomographic models for a broad depth range.

6. Tomographic Inversion

[40] The ray-theoretical sensitivity kernels adopted in this study do not account for finite frequency effects such

as scattering and wavefront healing effects. In order to consider these effects, finite frequency sensitivity kernels with the Born/Rytov approximation have been utilized in tomographic studies in the last decade [e.g., *Dahlen et al.*, 2000; *Montelli et al.*, 2004a, 2004b; *Ritzwoller et al.*, 2002; *Yoshizawa and Kennett*, 2005; *Zhou et al.*, 2006]. *Montelli et al.* [2004a] compared tomographic models from finite frequency and ray theories and found that the differences are small, particularly for medium to large velocity anomalies. The most remarkable improvement of the finite frequency inversion compared to the ray-theoretical one is in the form of 30–50% higher amplitudes of some velocity anomalies, specifically for small velocity anomalies.

[41] Our resolution tests show that jointly inverting different types of seismic data also helps to better recover the amplitudes of velocity anomalies compared to stand-alone inversions. Furthermore, *Sieminski et al.* [2004] asserted that theoretical shortcomings in ray theory tomography over finite frequency tomography can be overcome by using dense ray coverage or physically based regularization. *Boschi* [2006] and *van der Lee and Frederiksen* [2005] found that ray theory surface wave tomography is still valuable by showing little difference between ray theory results and finite frequency results for North America.

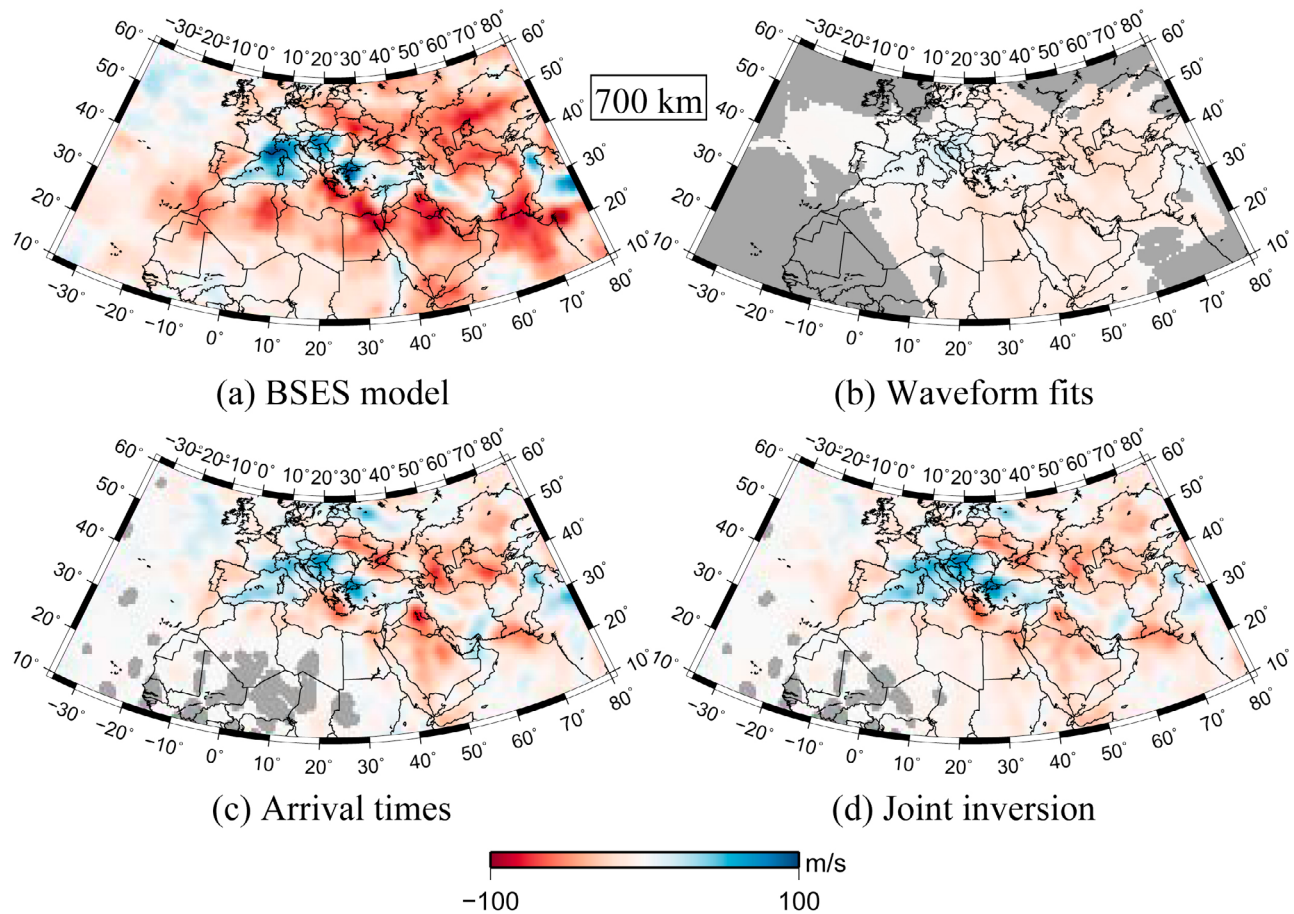


Figure 12. Resolution tests with noise contamination for S velocity perturbations at 700 km depth. The horizontal slices of S velocity perturbations (a) in the BSES model and inversion results with contaminated synthetic data (b) of waveform fits, (c) of arrival times, and (d) of the combined data sets are presented. Regions not covered by data sets are illustrated in gray.

[42] Because each of our data sets has relatively dense wave path coverage and because our strategy to invert them jointly allows better amplitude recovery, we believe that our use of ray-theoretical kernels in our inversions is entirely justified. In this paper we address the benefits of jointly inverting different types of data.

[43] Decades of literature on continent-scale seismic tomography as well as our own resolution tests, described in the previous section, show that high-frequency arrival times are sensitive to and have been used to image seismic anomalies of similar size and pattern as those imaged by regional waveform fits and group velocities. This may explain the observations of *Schmid et al.* [2004] that frequency dependence of body wave arrival times is not strong. The dominant scale of mantle heterogeneity seems too large to cause significant dispersion in teleseismic body waves. On the basis of these arguments, we assume that different data sets detect the same 3-D velocity structure.

[44] From the joint inversion for S velocity mantle structure along the Tethyan margin, variance reductions are obtained by 40% for teleseismic arrival times (40% for reprocessed ISC database and 73% for MCCC data),

87% for regional waveform fits, 72% for Rayleigh wave group velocities, and 80% for the independent Moho constraints. These variance reductions are relative to a one-dimensional model (MEAN) that is very close to the regional average. The large size of these variance reductions thus very nearly reflects the importance of 3-D structure in explaining the data rather than imperfections in the regional one-dimensional model. What is more striking about these variance reductions is that they are only 1–2% less than variance reductions obtained in stand-alone inversions of a single data set at a time, while the Moho constraints are 2% better matched in the joint inversion. This suggests that the aspects of 3-D structure sensed by one data set are very similar to those sensed by the other data sets. In other words, the different data sets are compatible and can be largely explained by the same 3-D structure. Weights in the joint inversion for teleseismic arrival times, waveform fits, Rayleigh wave group velocities, and independent Moho depth constraints are set to 1.0, 1.4, 1.8, and 4.0, respectively, through trial and error. These weights allow each data set to achieve similar variance reduction as in their stand-alone inversion.

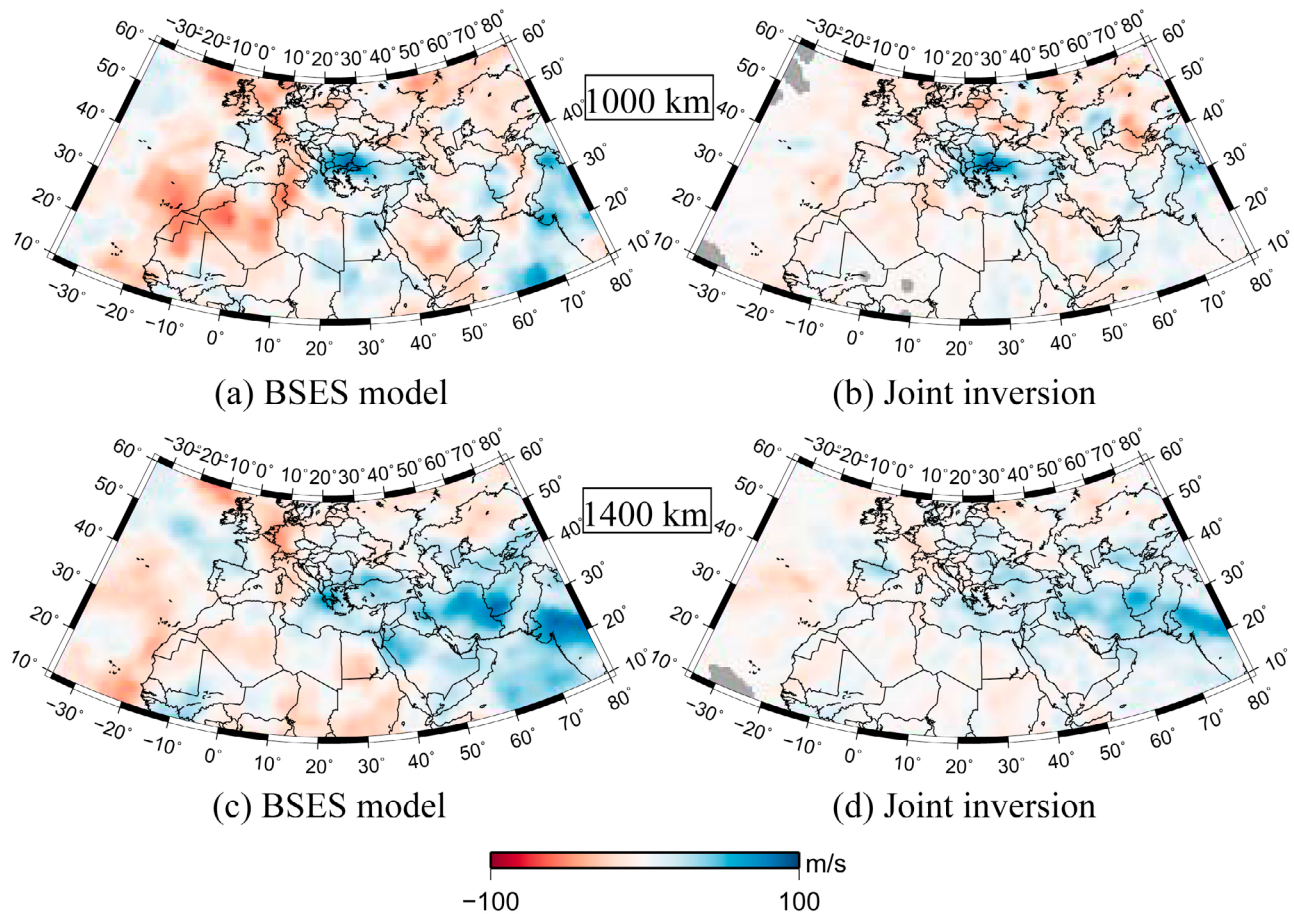


Figure 13. Resolution tests with noise contamination for S velocity perturbations at 1000 and 1400 km depths. The horizontal slices of S velocity perturbations in the BSES model at (a) 1000 and (c) 1400 km depths are presented on left and joint inversion results at (b) 1000 and (d) 1400 km depths on right. Regions not covered by data sets are illustrated in gray.

Every data set was fit to within approximately one standard deviation.

7. Results and Interpretation

[45] Overall, the Moho results from the joint inversion (Figure 15a) agree with the models of *Marone et al.* [2003] and *Schmid et al.* [2008] for the Mediterranean region, but also with the more independent and recently compiled maps of *Grad et al.* [2009] and *Tesauro et al.* [2008]. While the latter two are based on a larger set of Moho constraints than the former two, our Moho model extends further east and uniquely incorporates constraints on Moho depth from regional waveform fits and dispersion curves.

[46] Our Moho result is not very different from CRUST2.0 [*Bassin et al.*, 2000]. Differences exist for the Moho beneath the Bay of Biscay, the Cantabrian Mountains, North Africa, the Red Sea, and the Himalayas (see Figure 1). The data we used have limited resolving power for the Moho in the latter three regions, but reasonable resolution in the former two. The new Moho is consistent with the independent imaging, using teleseismic receiver function analysis, of a deeper Moho beneath the Cantabrian Mountains by *Diaz et al.* [2003]. These results suggesting that

indeed the Moho is shallower beneath the Bay of Biscay and deeper beneath the Cantabrian Mountains than in CRUST2.0. This accentuates the exceptional sharpness of the continent-ocean transition in northern Iberia, also observed in the bathymetry, and confirms the ability of the combined data sets to resolve sharp transitions.

[47] Map views of the new model (Figure 15) reveal low S velocity anomalies under thin crust beneath extensional back-arc basins such as the Alegro-Provençal and the Tyrrhenian basins in the western Mediterranean Sea and the Pannonian basin near the Carpathians. These back-arc basins have undergone the Late Neogene subsidence [*Cloetingh et al.*, 2007]. The Red Sea, which is undergoing extensional rifting [*Zeyen et al.*, 1997], also has a thin crust overlying a low-velocity uppermost mantle. In contrast, high-velocity uppermost mantle is found beneath the thin, oceanic crust of the eastern Atlantic Ocean and the Arabian Sea. The Ionian Sea also has a thin crust and is underlain by relatively high velocities, confirming the oceanic nature of this sea.

[48] Thick crust underlain by relatively low S velocities is detected beneath mountain belts such as the Anatolian plateau, the Iranian plateau, and the Hindu Kush, which are formed by continental collision. On the other hand, thick

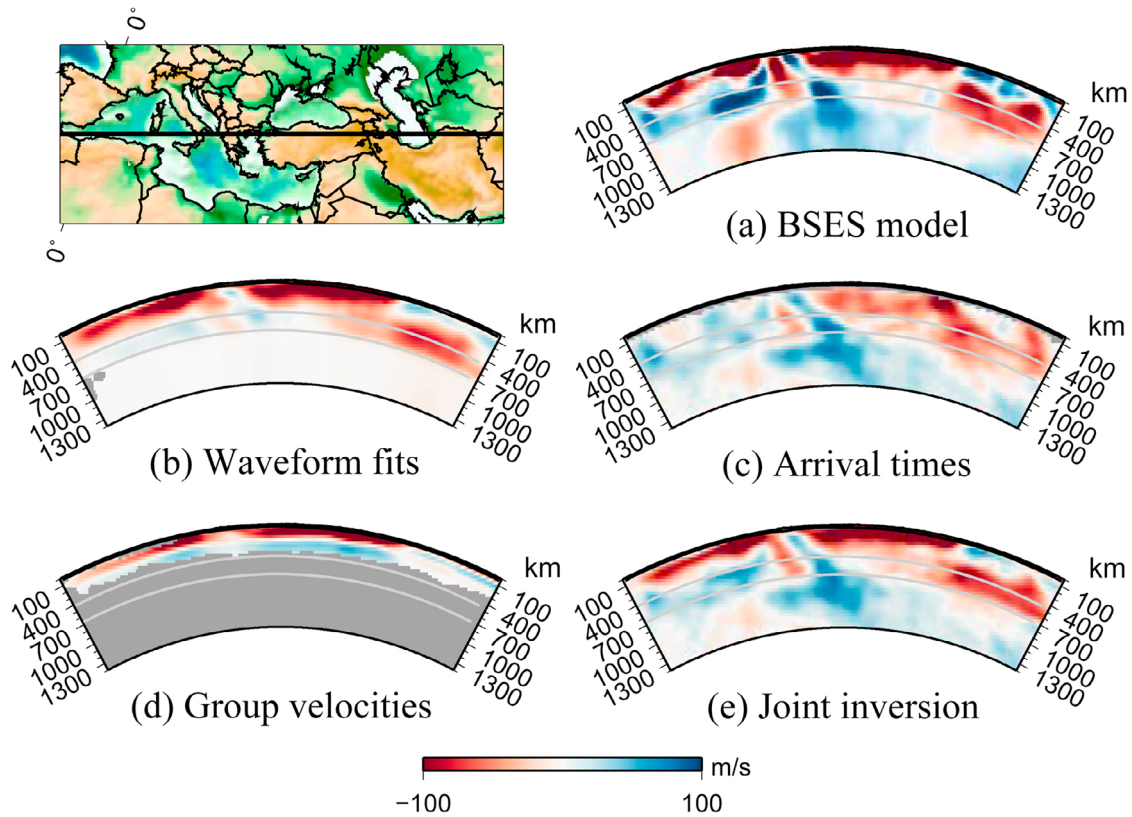


Figure 14. Cross-section maps encompassing the western Mediterranean Sea and the Hindu Kush. Discontinuities at 410 and 660 km depths are indicated in gray lines. The cross-section maps of S velocity perturbation in (a) the BSES model, inversion results with contaminated synthetic data of (b) waveform fits, (c) group velocities, (d) of arrival times, and (e) the combined data sets are presented. Regions not covered by data sets are illustrated in gray.

crust underlain by relatively high S velocities is observed underneath stable cratons like the East European platform and the Arabian platform. Surprisingly, the Arabian shield is different from typical shields and the Arabian platform in that it overlies a low-velocity mantle. *Daradich et al.* [2003] attribute this to rifting in the Red Sea. Figures 15b–15e suggest that the thickness of the East European platform’s lithosphere is about 150–200 km. Beneath the West African craton high-velocity anomalies are detected down to at least 150 km depth, but velocities at larger depths are not well resolved.

[49] In contrast, northeastern Africa is underlain by a pattern of relatively low-velocity anomalies. These relatively low velocities have some geographic affinity with regions of Cenozoic volcanic and rifting activity, for example, beneath Darfur, the Sirte basin, and Tibesti [*Liégeois et al.*, 2005; *Abadi et al.*, 2008; *Ebinger and Sleep*, 1998].

[50] Low-velocity anomalies at the mid-Atlantic ridge are detected down to at least 150 km depth. This depth is consistent with a number of previous results, including a recent one from finite frequency surface wave tomography [*Zhou et al.*, 2006]. Away from the ridge, the Atlantic Ocean is underlain by relatively high velocities down to about 100 km, and relatively low velocities deeper than 100 km, representing a typical oceanic lithosphere-asthenosphere system.

[51] The transition zone is characterized by a range of high-velocity anomalies as well as a few concentrated low-velocity anomalies. The high-velocity anomalies are distributed beneath the northern Mediterranean region from as far west as eastern Spain and the Alboran Sea to as far east as the Caucasus (Figure 15h). These anomalies most likely represent subducting slabs from regions such as the Apennines, the Calarian arc, the Carpathians, the Caucasus, and the Hellenic arc. An elongated high-velocity anomaly follows the Anatolian plateau, the Zagros belt, and the Deccan traps and exists as deep as 1400 km (Figure 15l), which is interpreted as the subducted Neo-Tethys Oceanic lithosphere by *Van der Voo et al.* [1999].

7.1. Subducted Lithosphere Beneath the Mediterranean Sea

[52] High seismic velocities of the subducting African lithosphere have been consistently imaged beneath the Hellenic arc since 1988 [*Bijwaard et al.*, 1998; *Piromallo and Morelli*, 2003; *Schmid et al.*, 2008; *Spakman et al.*, 1988, 1993]. Our work has also imaged this Hellenic slab (Figure 16a) and shows that it extends continuously from the surface down to 1400 km, confirming the longevity of this subduction zone and the associated penetration of the slab into the lower mantle found by *Spakman et al.* [1993].

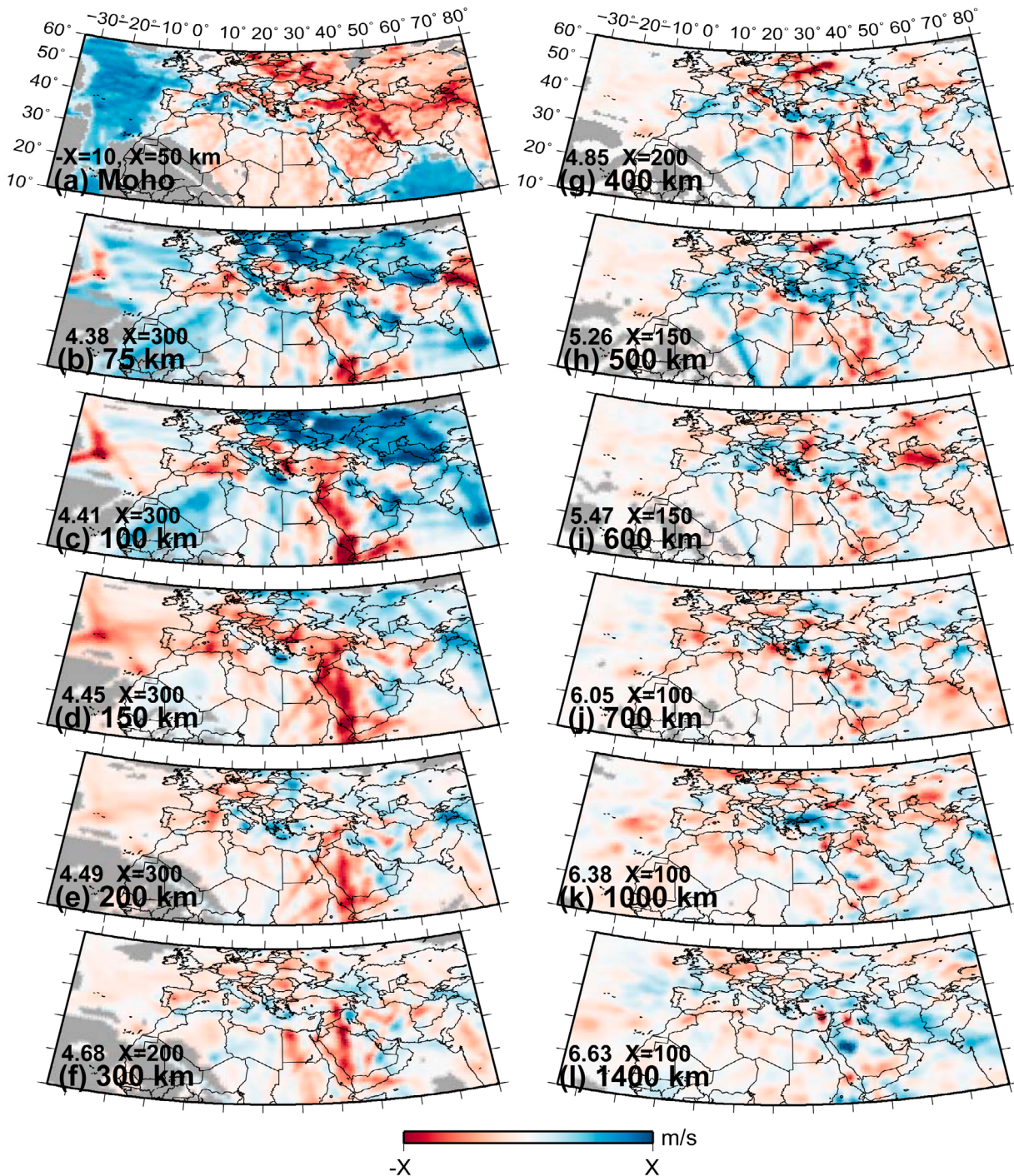


Figure 15. (a) The Moho depth distribution and the horizontal slices at (b) 75, (c) 100, (d) 150, (e) 200, (f) 300, (g) 400, (h) 500, (i) 600, (j) 700, (k) 1000, and (l) 1400 km depths from the joint inversion. Velocity perturbations are relative to the reference model “MEAN,” and the reference S velocity at each depth is written on the left side in km s^{-1} scale. Regions not covered by data sets are illustrated in gray.

Our results show that the width of the slab, although somewhat overestimated by typical seismic-tomographic “smearing,” does not vary significantly with depth within the upper mantle. However, the slab seems to widen abruptly just beneath 660 km in the lower mantle. This is in contrast to the tomographic model of *Piromallo and Morelli* [2003], which shows that the slab widening begins within

the transition zone. However, the widening particular to our model may well support the assertion of *Capitanio et al.* [2009] that the slab had been accumulated within the transition zone because of high viscosity in the lower mantle, triggering a slab avalanche that caused the imaged slab widening in the lower mantle.

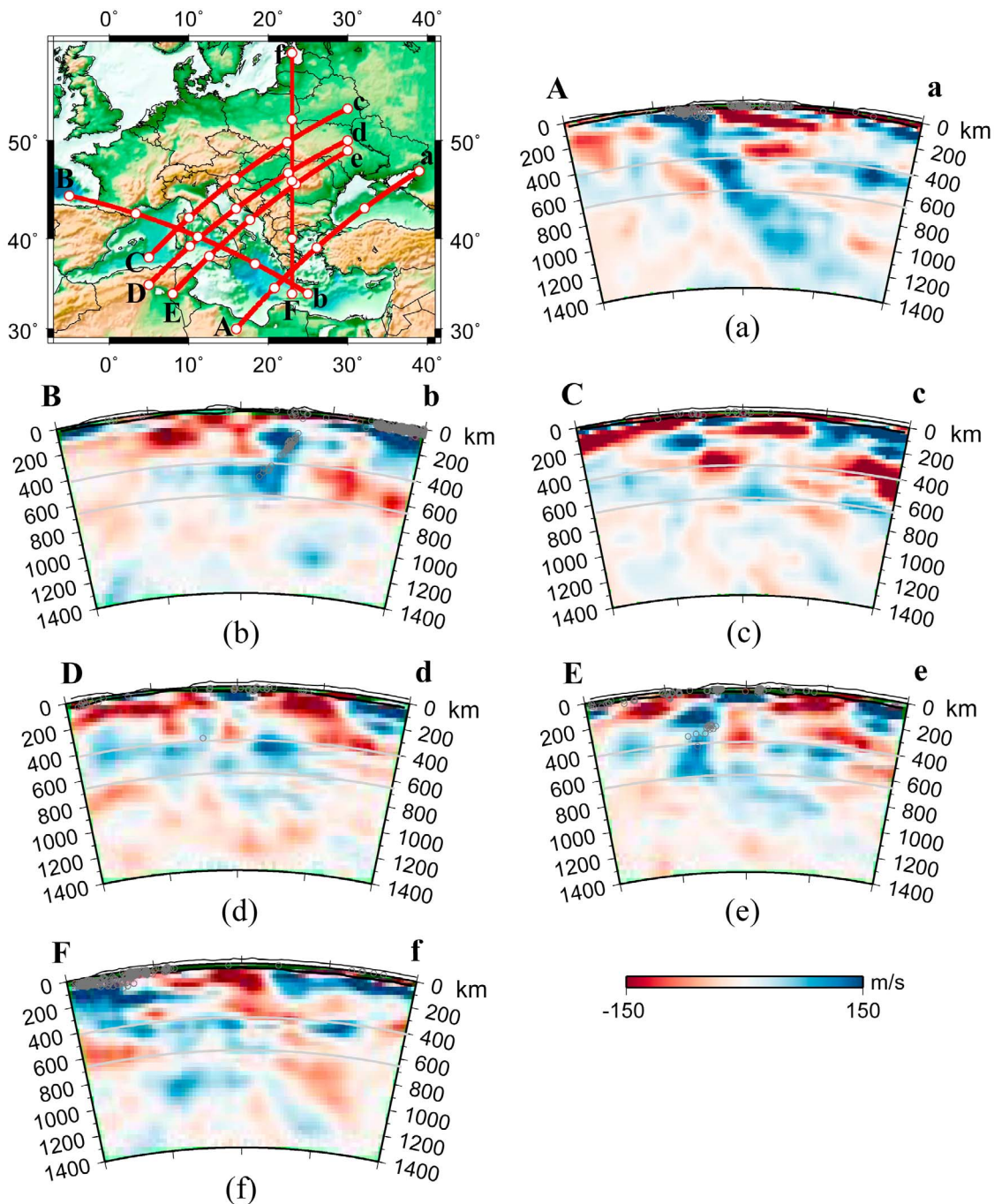


Figure 16. Vertical cross-section maps perpendicular to (a) the Hellenic arc, (b) the Calabrian arc, the Apennines (c–e) from north to south, and (f) from the Mediterranean Sea to the Baltic Sea. Moho depth and surface topography are shown in black solid lines. Topography is exaggerated 10 times. Dark gray open circles represent events, and light gray lines indicate 410 and 660 km discontinuities. Great circle paths corresponding to cross sections are indicated on the left-top map. White circles on the great circle paths correspond to ticks shown in the cross sections.

[53] We have also imaged the high-velocity, subducting lithosphere of the Ionian Sea beneath the Calabrian arc (Figure 16b) and find that it extends into the transition zone. The portion of this slab in the transition zone is flat and extends over about 1000 km to the NWW, presumably as a result of slab roll back [de Jonge *et al.*, 1994; Goes *et al.*, 2004; Gueguen *et al.*, 1998]. This roll back might have

been facilitated by the relatively high age of 180–200 Ma [Della Vedova and Pellis, 1989] and negative buoyancy of the Ionian lithosphere, which is likely also responsible for the steep dip of this Calabrian slab above the transition zone. This steep dip angle is in marked contrast to the much gentler dip angle of the adjacent Adriatic lithosphere that has been imaged beneath the Apennines (Figures 16c–16e).

Figures 16b and 16e illustrate how these two slabs might be interfering with each other in the uppermost mantle.

[54] The morphology of the Adriatic slabs beneath the Apennines has been the subject of debate. *Wortel and Spakman* [2000] proposed that slab detachment is progressing from north to south along the Apennines while *Lucente and Speranza* [2001] assert that the slab is partitioned into northern and southern slabs surrounding a central “slab window” as a result of cessation of subduction beneath the central Apennines. The latter scenario is also supported by Late Miocene uplift [*van der Meulen et al.*, 1999], Neogene-Quaternary magmatism [*Serri et al.*, 1993] in the central Apennines, and absence of intermediate earthquakes observed beneath the central Apennines [*Selvaggi and Amato*, 1992] while the former scenario is supported by distinct temporal depocenter shifts from north to south [*van der Meulen et al.*, 1998]. Our model shows a low-velocity anomaly at 100–200 km depth beneath the central Apennines, which is surrounded by high-velocity anomalies (Figure 15 and Figure 16d). This geometry is consistent with Lucente and Speranza’s inference of a central slab window. However, our results are not inconsistent with the inferences of *Wortel and Spakman* [2000] because our image of the Adriatic slab is less continuous in the north (Figure 16c) than in the south (Figure 16e).

7.2. Pannonian Basin

[55] Our joint inversion confirms results from previous studies [*Horváth*, 1993; *Marone et al.*, 2003, 2004; *Schmid et al.*, 2008; *Wortel and Spakman*, 2000] that imaged a relatively shallow Moho (<25 km) with a low-velocity anomaly at subcrustal depth beneath the Pannonian basin (Figure 15a–15d). *Horváth* [1993] and *Royden* [1988] argue that this basin was formed in a back-arc setting, while *Burov and Cloetingh* [2009], *Huismans et al.* [2001], and *Hoernle et al.* [1995] argue for an active mantle upwelling preceded by passive extension and for a mantle plume source for some of the basin’s igneous rocks. This implies that the low-velocity anomaly would originate from a source deeper than the asthenosphere. This shallow low-velocity anomaly beneath the Pannonian basin (Figure 16d) appears to extend more deeply along a slightly twisted path that has the anomaly dipping to the east within the upper mantle and turns to the northeast in the transition zone (Figures 15b–15h and Figures 16c–16f). The deeper part of this low-velocity anomaly is the low-velocity anomaly at depth of 400–500 km beneath the East European platform (Figure 15g–15h) that has been interpreted as a hydrated part of the mantle by *Nolet and Zielhuis* [1994]. The low-velocity anomaly may be connected to even deeper low-velocity structures in the lower mantle (Figure 16f), but the data’s resolving power remains inconclusive on this (Figure 8c).

7.3. Zagros Belt and Iranian Plateau

[56] The Arabian and Eurasian plates collided in Oligo-Miocene times [*Koop and Stoneley*, 1982] and the lithosphere of the Arabian plate was subducted below the Eurasian plate along the Zagros belt. This subducted lithosphere is, however, surprisingly inactive seismically [*Tatar et al.*, 2004].

[57] In our model various dispositions of high- and low-velocity anomalies exhibit complex tectonic structure beneath

the Zagros belt (Figures 17a–17c). While Figures 17b and 17c show the Zagros belt being underlain by dipping high-velocity anomalies that could be interpreted as subducted lithosphere of the trailing fragments of the Neo-Tethys Ocean, Figure 17a is devoid of such high velocities. This contrast might indicate a slab detachment process, somewhat analogous to that inferred beneath the Apennines, which started beneath the northern Zagros belt and may be progressing southward.

[58] The Iranian plateau directly adjacent to the Zagros belt is underlain, like the Anatolian plateau, by low *S* velocities down to just over 150 km (Figures 15b–15d and 17a–17c). *Alinaghi et al.* [2007], *Maggi and Priestley* [2005], and *Kaviani et al.* [2007], for example, also found this low-velocity anomaly beneath the Iranian plateau, as well as the high-velocity anomalies beneath the Zagros belt. The low velocities under central Iran continue east beneath the Lut block (Figures 15b–15d). The low-velocity anomaly underneath the Lut block extends down and northward to at least the transition zone where a large low-velocity anomaly exists, roughly beneath Turkmenistan (Figures 15i, 17c, and 17d). This low velocity beneath Turkmenistan might be the result of a relatively hot or a relatively hydrated transition zone. The low-velocity anomaly may be connected to a more subdued low-velocity structure in the top of the lower mantle (Figure 17c). The remainder of the lower mantle in this region is dominated by high-velocity anomalies (Figures 17b–17c), which are thought to be subducted Neo-Tethys lithosphere. This Neo-Tethys lithosphere could present a ready source of water that might have hydrated the low-velocity transition zone beneath Turkmenistan following a water cycle such as described by *van der Lee et al.* [2008]. Such hydration would be greatly facilitated by the high water solubility of the transition zone [*Smyth*, 1987]. It is indeed possible that this deep source of low-velocity mantle has welled up to the uppermost mantle beneath the Lut block because Pliocene-Quaternary volcanic rocks in eastern Iran have an overall signature similar to that of ocean island basalts [*Walker et al.*, 2009], which would require a deep magmatic source.

8. Conclusions

[59] We find that regional *S* and Rayleigh waveform fits, teleseismic *S* and *SKS* arrival times, fundamental mode Rayleigh wave group velocity measurements, and independent Moho depth constraints are compatible and can be largely explained by the same 3-D structure. Joint inversion of these different data sets for a 3-D *S* velocity model along the Tethyan margin simultaneously explains the different types of seismic data to within approximately one standard deviation. This joint inversion model is better resolved than models from stand-alone inversions of individual data sets. Resolution tests with various models confirm that the joint inversion yields good resolution ranging from the Moho down to 1400 km depth for the bulk of the study region. For some regions, such as the eastern Atlantic Ocean, the Arabian Sea, and North Africa, good resolution is confined to the uppermost mantle.

[60] The joint inversion Moho map is enhanced from previous maps [*Marone et al.*, 2003; *Schmid et al.*, 2008] in

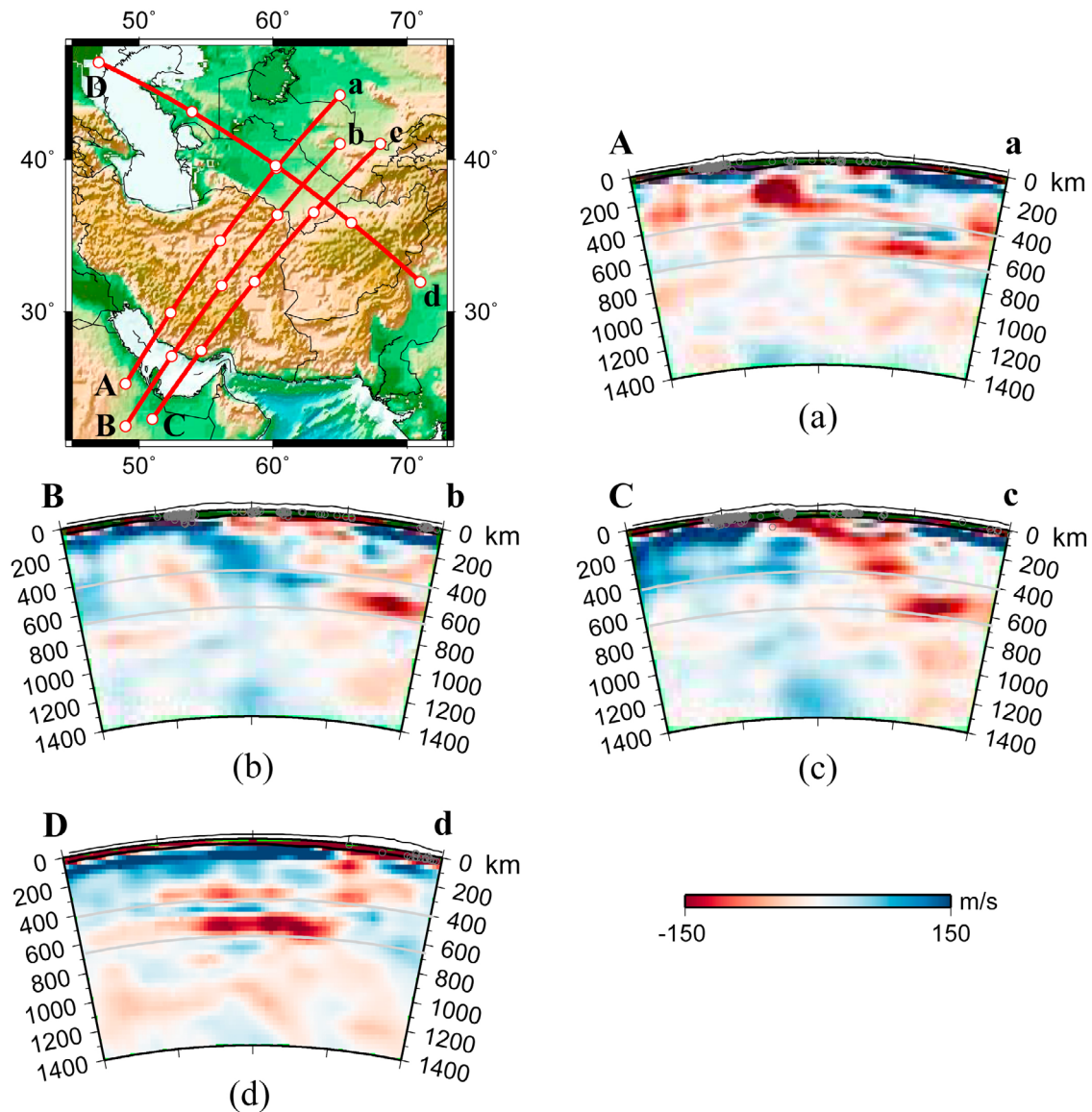


Figure 17. Vertical cross-section maps perpendicular to the Zagros belt (a–c) from north to south and (d) from the Caspian Sea to northern India. Moho depth and surface topography are shown in black solid lines. Topography is exaggerated 10 times. Dark gray open circles represent events, and light gray lines indicate 410 and 660 km discontinuities. Great circle paths corresponding to cross sections are indicated on the left-top map. White circles on the great circle paths correspond to ticks shown in the cross sections.

that it extends further south and east and also because it is additionally constrained by the group velocity data. More recent Moho maps [Grad *et al.*, 2009; Tesauro *et al.*, 2008] extend further to the north than ours, but not as far south [Grad *et al.*, 2009] and considerably less to the east and west [Tesauro *et al.*, 2008]. Both these maps are based on impressive compilations of a vast literature on local crustal studies. While Tesauro and coworkers' map is part of a more comprehensive crustal model that includes representative P velocities, our joint inversion map has the benefit of being simultaneously constrained by a variety of different data sets for the same region.

[61] Typical oceanic structure, a thin crust over a rigid mantle, is found beneath the Atlantic Ocean, the Arabian Sea, and the Ionian Sea. The rigid lithospheric mantle

extends to roughly 100 km depth and overlies a typical low-velocity region, the asthenosphere. Thin crust over a weak mantle is found beneath extensional regions such as the Gulf of Aden, the Red Sea, the Tyrrhenian Sea, the Alegero-Provençal basin, and the Pannonian basin. The low velocities beneath the Pannonian basin appear to extend as deeply as the transition zone, but whether or not it is related to a lower-mantle plume remains ambiguous. Typical continental-platform structure, thick crust over rigid mantle, is found beneath the East European platform and the Arabian platform. West Africa also shows the rigid mantle but its Moho is not well resolved by our data sets. Some regions of tectonic collision and compression, such as the Anatolian plateau, the Iranian plateau, and the Hindu Kush, show thick crust over weak mantle. Beneath the Iranian plateau, the low

velocities of this weak mantle seem to extend as deeply as the transition zone beneath Turkmenistan and possibly deeper. Northeastern Africa shows a thick crust over alternating patches of rigid and weak mantle. The rigid patches may reflect typical platform structure while the weak patches may be related to various rifting and hot spot activities.

[62] The transition zone is dominated by a range of high-velocity anomalies, representing various fragments of subducted and subducting lithosphere. The subducting Hellenic slab is imaged as a high-velocity anomaly that continues from the surface down to 1400 km, below which the data lose resolving power. The Calabrian slab does not seem to continue into the lower mantle and its portion in the transition zone is flat for about a 1000 km. The seismically inactive Apenninic slab, however, seems to extend into the upper mantle for only a few hundreds of kilometers, and is not continuous along the Apennines. Somewhat analogously the seismically inactive Zagros slab also seems discontinuous along the Zagros belt but extends more deeply down to the transition zone. This slab represents subducted lithosphere from the Neo-Tethys Ocean and may have released water into the transition zone beneath Turkmenistan.

[63] This study has shown that multiple different data sets can be successfully combined into a high-resolution tomographic model. The utility of tomographic models for explaining and predicting a variety of observations and dynamics is greatly increased by reducing disparities in resolving power. This study's resolving power has reduced such disparities through combining several different, large seismic data sets with complementary as well as overlapping resolving power.

[64] **Acknowledgments.** We thank Walter Mooney and Anne Paul for sharing their Moho data set and Margaret Benoit, Andrew Nyblade, and Yongcheol Park for sharing their relative arrival time data sets from Arabia and Ethiopia. We also thank E. Robert Engdahl for providing the reprocessed ISC database. Raiden Hasegawa, Ryan Lange, and Xiaoting Lou helped us to get relative arrival time data at central Asia and Turkey. An anonymous reviewer reminded us to correct group velocities for the ocean water layer, thank you. All figures were created using Generic Mapping Tools (GMT) [Wessel and Smith, 1998]. This work was supported by the Korea Research Foundation grant KRF-2006-214-C00092 funded by the Korean Government (MOEHRD) and the U.S. DOE under contract DE-FC52-04NA25541. This work was performed under the auspices of the U.S. Department of Energy by Lawrence Livermore National Laboratory under contract DE-AC52-07NA27344. This is LLNL contribution LLNL-JRNL-422305.

References

- Abadi, A. M., J.-D. van Wees, P. M. van Dijk, and S. A. P. L. Cloetingh (2008), Tectonics and subsidence evolution of the Sirt Basin, Libya, *AAPG Bull.*, *92*, 993–1027, doi:10.1306/03310806070.
- Agnew, D. C., J. Berger, W. E. Farrell, J. F. Gilbert, G. Masters, and D. Miller (1986), Project IDA: A decade in review, *Eos Trans. AGU*, *67*, 203–216.
- Al-Amri, M., and A. Al-Amri (1999), Configuration of the seismographic networks in Saudi Arabia, *Seismol. Res. Lett.*, *70*, 322–331.
- Al-Damegh, K., E. Sandvol, and M. Barazangi (2005), Crustal structure of the Arabian plate: New constraints from the analysis of teleseismic receiver functions, *Earth Planet. Sci. Lett.*, *231*, 177–196, doi:10.1016/j.epsl.2004.12.020.
- Al-Lazki, A. I., D. Seber, E. Sandvol, and M. Barazangi (2002), A crustal transect across the Oman mountains of the eastern margin of Arabia, *GeoArabia*, *7*, 47–78.
- Alinaghi, A., I. Koulakov, and H. Thybo (2007), Seismic tomographic imaging of *P*- and *S*-waves velocity perturbations in the upper mantle beneath Iran, *Geophys. J. Int.*, *169*, 1089–1102, doi:10.1111/j.1365-246X.2007.03317.x.
- Almond, D. C. (1986), Geological evolution of the Afro-Arabian dome, *Tectonophysics*, *131*, 301–332, doi:10.1016/0040-1951(86)90180-0.
- Baer, M. (1990), The seismic station network of the Swiss Seismological Service, in *International Workshop on MEDNET, the Broad-Band Seismic Network for the Mediterranean*, edited by E. Boschi, D. Giardini, and A. Morelli, pp. 345–350, *Ist. Naz. Geofis.*, Rome.
- Bassin, C., G. Laske, and G. Masters (2000), The current limits of resolution for surface wave tomography in North America, *Eos Trans. AGU*, *81* (48), Fall Meet. Suppl., Abstract S12A-03.
- Baumgardner, R. B., and P. O. Frederickson (1985), Icosahedral discretization of the two-sphere, *SIAM J. Numer. Anal.*, *22*, 1107–1115, doi:10.1137/0722066.
- Benoit, M. H., A. A. Nyblade, T. J. Owens, and G. Stuart (2006), Mantle transition zone structure and upper mantle *S* velocity variations beneath Ethiopia: Evidence for a broad, deep-seated thermal anomaly, *Geochem. Geophys. Geosyst.*, *7*, Q11013, doi:10.1029/2006GC001398.
- Bijwaard, H., W. Spakman, and E. R. Engdahl (1998), Closing the gap between regional and global travel time tomography, *J. Geophys. Res.*, *103*, 30,055–30,078, doi:10.1029/98JB02467.
- Bird, P. (2003), An updated digital model of plate boundaries, *Geochem. Geophys. Geosyst.*, *4*(3), 1027, doi:10.1029/2001GC000252.
- Bohannon, R. G., C. W. Naeser, D. L. Schmidt, and R. A. Zimmermann (1989), The timing of uplift, volcanism and rifting peripheral to the Red Sea: A case for passive rifting? *J. Geophys. Res.*, *94*, 1683–1701, doi:10.1029/JB094iB02p01683.
- Boschi, E., D. Giardini, and A. Morelli (1991), MedNet: The very broad-band seismic network for the Mediterranean, *Nuovo Cim.*, *14*, 79–99, doi:10.1007/BF02509260.
- Boschi, L. (2006), Global multiresolution models of surface wave propagation: Comparing equivalently regularized Born and ray theoretical solutions, *Geophys. J. Int.*, *167*, 238–252, doi:10.1111/j.1365-246X.2006.03084.x.
- Burov, E., and S. Cloetingh (2009), Controls of mantle plumes and lithospheric folding on modes of intraplate continental tectonics: Differences and similarities, *Geophys. J. Int.*, *178*, 1691–1722, doi:10.1111/j.1365-246X.2009.04238.x.
- Camp, V. E., and M. J. Roobol (1992), Upwelling asthenosphere beneath western Arabia and its regional implications, *J. Geophys. Res.*, *97*, 15,255–15,271, doi:10.1029/92JB00943.
- Capitani, F. A., C. Faccenna, and R. Funicello (2009), The opening of Sirte basin: Result of slab avalanching? *Earth Planet. Sci. Lett.*, *285*, 210–216, doi:10.1016/j.epsl.2009.06.019.
- Cloetingh, S. A. P. L., et al. (2007), TOPO-EUROPE: The geoscience of coupled deep Earth-surface processes, *Global Planet. Change*, *58*, 1–118, doi:10.1016/j.gloplacha.2007.02.008.
- Constable, S. C., R. L. Parker, and C. G. Constable (1987), Occam's inversion: A practical algorithm for generating smooth models from electromagnetic sounding data, *Geophysics*, *52*, 289–300, doi:10.1190/1.1442303.
- Crough, S. T. (1979), Hotspot epeirogeny, *Tectonophysics*, *61*, 321–333, doi:10.1016/0040-1951(79)90304-4.
- Dahlen, F. A., S.-H. Hung, and G. Nolet (2000), Fréchet kernels for finite-frequency traveltimes—I. Theory, *Geophys. J. Int.*, *141*, 157–174, doi:10.1046/j.1365-246X.2000.00070.x.
- Daradich, A., J. X. Mitrovica, R. N. Pysklywec, S. D. Willett, and A. M. Forte (2003), Mantle flow, dynamic topography, and rift-flank uplift of Arabia, *Geology*, *31*, 901–904, doi:10.1130/G19661.1.
- de Jonge, M. R., M. J. R. Wortel, and W. Spakman (1994), Regional scale tectonic evolution and the seismic velocity structure of the lithosphere and upper mantle: The Mediterranean region, *J. Geophys. Res.*, *99*, 12,091–12,108, doi:10.1029/94JB00648.
- Della Vedova, B., and G. Pellis (1989), New heat flow density measurements in the Ionian sea, paper presented at VIII Convegno, Gruppo Naz. di Geofis. della Terra Solida, Rome.
- Dercourt, J., et al. (1986), Geological evolution of the Tethys Belt from the Atlantic to the Pamirs since the Lias, *Tectonophysics*, *123*, 241–315, doi:10.1016/0040-1951(86)90199-X.
- Dewey, J., M. Helman, E. Turco, D. Hutton, and S. Knott (1989), Kinematics of the western Mediterranean, in *Alpine Tectonics*, edited by M. Coward, D. Dietrich, and R. Park, *Geol. Soc. Spec. Publ.*, *45*, 265–283.
- Diaz, J., J. Gallart, D. Pedreira, J. A. Pulgar, M. Ruiz, C. López, and J. M. González-Cortina (2003), Teleseismic imaging of alpine crustal underthrusting beneath Niberia, *Geophys. Res. Lett.*, *30*(11), 1554, doi:10.1029/2003GL017073.
- Dongarra, J. J., C. B. Moler, J. R. Bunch, and G. W. Stewart (1979), *LINPACK Users' Guide*, 320 pp., Soc. for Ind. and Appl. Math., Philadelphia, Pa.
- Dziewonski, A. M., J. Bloch, and M. Landisman (1969), A new technique for the analysis of transient seismic signals, *Bull. Seismol. Soc. Am.*, *59*, 427–444.
- Dziewonski, A. M., G. Ekström, and M. Salganik (1994), Centroid-moment tensor solutions for January–March 1994, *Phys. Earth Planet. Inter.*, *86*, 253–261, doi:10.1016/0031-9201(94)90124-4.

- Ebinger, C. J., and N. H. Sleep (1998), Cenozoic magmatism throughout east Africa resulting from impact of a single plume, *Nature*, *395*, 788–791, doi:10.1038/27417.
- Engdahl, E. R., R. Van der Hilst, and R. Buland (1998), Global teleseismic earthquake relocation with improved travel times and procedures for depth determination, *Bull. Seismol. Soc. Am.*, *88*, 722–743.
- Gitterman, Y., V. Pinsky, and A. Shapira (1998), Spectral classification methods in monitoring small local events by the Israel seismic network, *J. Seismol.*, *2*, 237–256, doi:10.1023/A:1009738721893.
- Goes, S., D. Giardini, S. Jenny, C. Hollenstein, H.-G. Kahle, and A. Geiger (2004), A recent tectonic reorganization in the south-central Mediterranean, *Earth Planet. Sci. Lett.*, *226*, 335–345, doi:10.1016/j.epsl.2004.07.038.
- Grad, M., T. Tiira, and the ESC Working Group (2009), The Moho depth map of the European Plate, *Geophys. J. Int.*, *176*, 279–292, doi:10.1111/j.1365-246X.2008.03919.x.
- Gueguen, E., C. Doglioni, and M. Fernandez (1998), On the post-25 Ma geodynamic evolution of the western Mediterranean, *Tectonophysics*, *298*, 259–269, doi:10.1016/S0040-1951(98)00189-9.
- Hanka, W. (1990), The German Regional Broadband Seismic Network (GRN) Project, in *International Workshop on MEDNET, the Broad-Band Seismic Network for the Mediterranean*, edited by E. Boschi, D. Giardini, and A. Morelli, pp. 83–95, Ist. Naz. di Geofis., Rome.
- Hanka, W., and R. Kind (1994), The GEOFON program, *IRIS Newsl.*, *13*, 1–4.
- Harjes, H. P., and D. Seidl (1978), Digital recording and analysis of broadband seismic data at the Gräfenberg (GRF) array, *J. Geophys. Res.*, *44*, 511–523.
- Herrmann, R. B. (1973), Some aspects of band-pass filtering of surface waves, *Bull. Seismol. Soc. Am.*, *63*, 663–671.
- Hoernle, K., Y. Zhang, and D. Graham (1995), Seismic and geochemical evidence for large-scale mantle upwelling beneath the eastern Atlantic and western and central Europe, *Nature*, *374*, 34–39, doi:10.1038/374034a0.
- Horváth, F. (1993), Toward a mechanical model for the formation of the Pannonian Basin, *Tectonophysics*, *226*, 333–357, doi:10.1016/0040-1951(93)90126-5.
- Huisman, R. S., Y. Y. Podladchikov, and S. Cloetingh (2001), Dynamic modeling of the transition from passive to active rifting, application to the Pannonian basin, *Tectonics*, *20*, 1021–1039, doi:10.1029/2001TC900010.
- Julià, J., and J. Mejía (2004), Thickness and Vp/Vs ratio variation in the Iberian crust, *Geophys. J. Int.*, *156*, 59–72, doi:10.1111/j.1365-246X.2004.02127.x.
- Kavian, A., A. Paul, E. Bourova, D. Hatzfeld, H. Pedersen, and M. Mokhtari (2007), A strong seismic velocity contrast in the shallow mantle across the Zagros collision zone (Iran), *Geophys. J. Int.*, *171*, 399–410, doi:10.1111/j.1365-246X.2007.03535.x.
- Kennett, B. L. N., and E. R. Engdahl (1991), Traveltimes for global earthquake location and phase identification, *Geophys. J. Int.*, *105*, 429–465, doi:10.1111/j.1365-246X.1991.tb06724.x.
- Koop, W. J., and R. Stoneley (1982), Subsidence history of the Middle East Zagros Basin, Permian to recent, *Philos. Trans. R. Soc. London, Ser. A*, *305*, 149–168, doi:10.1098/rsta.1982.0031.
- Koulakov, I., M. K. Kaban, M. Tesauro, and S. Cloetingh (2009), P- and S-velocity anomalies in the upper mantle beneath Europe from tomographic inversion of ISC data, *Geophys. J. Int.*, *179*, 345–366, doi:10.1111/j.1365-246X.2009.04279.x.
- Kumar, M. R., D. S. Ramesh, J. Saul, D. Sarkar, and R. Kind (2002), Crustal structure and upper mantle stratigraphy of the Arabian shield, *Geophys. Res. Lett.*, *29*(8), 1242, doi:10.1029/2001GL014530.
- Levshin, A. L., V. F. Pisarenko, and G. A. Pogrebinsky (1972), On a frequency-time analysis of oscillations, *Ann. Geophys.*, *28*, 211–218.
- Li, X., G. Bock, A. Vafidis, R. Kind, H.-P. Harjes, W. Hanka, K. Wylegalla, M. Van der Meijde, and X. Yuan (2003), Receiver function study of the Hellenic subduction zone: Imaging crustal thickness variations and the oceanic Moho of the descending African lithosphere, *Geophys. J. Int.*, *155*, 733–748, doi:10.1046/j.1365-246X.2003.02100.x.
- Liégeois, J.-P., A. Benhallou, A. Azzouini-Sekkal, R. Yahiaoui, and B. Bonin (2005), The Hoggar swell and volcanism: Reactivation of the Precambrian Tuareg shield during Alpine convergence and West African Cenozoic volcanism, in *Plates, Plumes, and Paradigms*, edited by G. R. Foulger et al., *Spec. Pap. Geol. Soc. Am.*, *388*, 379–400, doi:10.1130/0-8137-2388-4.379.
- Lucente, F. P., and F. Speranza (2001), Belt bending driven by lateral bending of subducting lithospheric slab: Geophysical evidences from the northern Apennines (Italy), *Tectonophysics*, *337*, 53–64, doi:10.1016/S0040-1951(00)00286-9.
- Maggi, A., and K. Priestley (2005), Surface waveform tomography of the Turkish-Iranian plateau, *Geophys. J. Int.*, *160*, 1068–1080, doi:10.1111/j.1365-246X.2005.02505.x.
- Marone, F., M. Van der Meijde, S. Van der Lee, and D. Giardini (2003), Joint inversion of local, regional and teleseismic data for crustal thickness in the Eurasia-Africa plate boundary region, *Geophys. J. Int.*, *154*, 499–514, doi:10.1046/j.1365-246X.2003.01973.x.
- Marone, F., S. Van der Lee, and D. Giardini (2004), Three-dimensional upper-mantle S-velocity model for the Eurasia-Africa plate boundary region, *Geophys. J. Int.*, *158*, 109–130, doi:10.1111/j.1365-246X.2004.02305.x.
- Mohsen, A., R. Hofstetter, G. Bock, R. Kind, M. Weber, K. Wylegalla, and G. Rumpker, and the DESERT Group (2005), A receiver function study across the Dead Sea Transform, *Geophys. J. Int.*, *160*, 948–960, doi:10.1111/j.1365-246X.2005.02534.x.
- Mooney, W., C. Prodehl, and N. Pavlenkova (2002), Seismic velocity structure of the continental lithosphere from controlled source data, in *International Handbook of Earthquake and Engineering Seismology, Int. Geophys. Ser.*, vol. 81A, edited by W. H. K. Lee et al., pp. 887–910, Academic, Amsterdam, doi:10.1016/S0074-6142(02)80261-3.
- Montelli, R., G. Nolet, G. Masters, F. A. Dahlen, and S.-H. Hung (2004a), Global P and PP traveltimes tomography: Rays versus waves, *Geophys. J. Int.*, *158*, 637–654, doi:10.1111/j.1365-246X.2004.02346.x.
- Montelli, R., G. Nolet, F. A. Dahlen, G. Masters, E. R. Engdahl, and S.-H. Hung (2004b), Finite-frequency tomography reveals a variety of plumes in the mantle, *Science*, *303*, 338–343, doi:10.1126/science.1092485.
- Nolet, G. (1990), Partitioned waveform inversion and two-dimensional structure under the network of autonomously recording seismographs, *J. Geophys. Res.*, *95*, 8499–8512, doi:10.1029/JB095iB06p08499.
- Nolet, G., and A. Zielhuis (1994), Low S velocities under the Tornquist-Teisseyre zone: Evidence for water injection into the transition zone by subduction, *J. Geophys. Res.*, *99*, 15,813–15,820, doi:10.1029/94JB00083.
- Paige, C. C., and M. A. Saunders (1982a), LSQR: An algorithm for sparse linear equations and sparse least squares, *Trans. Math. Software*, *8*, 43–71, doi:10.1145/355984.355989.
- Paige, C. C., and M. A. Saunders (1982b), LSQR: Sparse linear equations and least squares problems, *Trans. Math. Software*, *8*, 195–209, doi:10.1145/355993.356000.
- Park, Y., A. A. Nyblade, A. J. Rodgers, and A. Al-Amri (2007), Upper mantle structure beneath the Arabian Peninsula and northern Red Sea from teleseismic body wave tomography: Implication for the origin of Cenozoic uplift and volcanism in the Arabian Shield, *Geochem. Geophys. Geosyst.*, *8*, Q06021, doi:10.1029/2006GC001566.
- Pasyanos, M. E. (2005), A variable-resolution surface wave dispersion study of Eurasia, North Africa, and surrounding regions, *J. Geophys. Res.*, *110*, B12301, doi:10.1029/2005JB003749.
- Pasyanos, M. E., and W. R. Walter (2002), Crustal and upper-mantle structure of North Africa, Europe and the Middle East from inversion of surface waves, *Geophys. J. Int.*, *149*, 463–481, doi:10.1046/j.1365-246X.2002.01663.x.
- Pasyanos, M. E., W. R. Walter, and S. E. Hazler (2001), A surface wave dispersion study of the Middle East and North Africa for monitoring the Comprehensive Nuclear-Test-Ban Treaty, *Pure Appl. Geophys.*, *158*, 1445–1474, doi:10.1007/PL00001229.
- Paul, A., A. Kavian, D. Hatzfeld, J. Vergne, and M. Mokhtari (2006), Seismological evidence for crustal-scale thrusting in the Zagros mountain belt (Iran), *Geophys. J. Int.*, *166*, 227–237, doi:10.1111/j.1365-246X.2006.02920.x.
- Paulssen, H. (1992), NARS-DEEP: NARS deployed on the East European Platform, *Europrobe News*, *1*, 9.
- Peter, D., L. Boschi, F. Deschamps, B. Fry, G. Ekström, and D. Giardini (2008), A new finite-frequency shear-velocity model of European-Mediterranean region, *Geophys. Res. Lett.*, *35*, L16315, doi:10.1029/2008GL034769.
- Peterson, J., and C. R. Hutt (1989), IRIS/USGS plans for upgrading the Global Seismograph Network, *U.S. Geol. Surv. Open File Rep.*, *89-471*, 46 pp.
- Piomallo, C., and A. Morelli (2003), P wave tomography of the mantle under the Alpine-Mediterranean area, *J. Geophys. Res.*, *108*(B2), 2065, doi:10.1029/2002JB001757.
- Ritsema, J., and H. van Heijst (2000), New seismic model of the upper mantle beneath Africa, *Geology*, *28*, 63–66, doi:10.1130/0091-7613(2000)28<63:NSMOTU>2.0.CO;2.
- Ritzwoller, M. H., and A. L. Levshin (1998), Eurasian surface wave tomography: Group velocities, *J. Geophys. Res.*, *103*, 4839–4878, doi:10.1029/97JB02622.
- Ritzwoller, M. H., N. M. Shapiro, M. P. Barmin, and A. L. Levshin (2002), Global surface wave diffraction tomography, *J. Geophys. Res.*, *107*(B12), 2335, doi:10.1029/2002JB001777.
- Rodi, W. L., P. Glover, T. M. C. Li, and S. S. Alexander (1975), A fast, accurate method for computing group velocity partial derivatives for Rayleigh and Love modes, *Bull. Seismol. Soc. Am.*, *65*, 1105–1114.

- Röhm, A. H. E., H. Bijwaard, W. Spakman, and J. Trampert (2000), Effects of arrival time errors on traveltimes tomography, *Geophys. J. Int.*, *142*, 270–276, doi:10.1046/j.1365-246x.2000.00145.x.
- Romanowicz, B., M. Cara, J. F. Fels, and D. Rouland (1984), Geoscope; a French initiative in long-period three-component global seismic networks, *Eos Trans. AGU*, *65*, 753–754.
- Royden, L. H. (1988), Late Cenozoic tectonics of the Pannonian Basin system, in *The Pannonian Basin: A Study in Basin Evolution*, edited by L. Royden and F. Horváth, *AAPG Mem.*, *45*, 27–48.
- Sandvol, E., D. Seber, M. Barazangi, F. Vernon, R. Mellors, and A. Al-Amri (1998), Lithospheric seismic velocity discontinuities beneath the Arabian shield, *Geophys. Res. Lett.*, *25*, 2873–2876, doi:10.1029/98GL02214.
- Schivardi, R., and A. Morelli (2009), Surface wave tomography in the European and Mediterranean region, *Geophys. J. Int.*, *177*, 1050–1066, doi:10.1111/j.1365-246X.2009.04100.x.
- Schmid, C., S. Van der Lee, and D. Giardini (2004), Delay times and shear wave splitting in the Mediterranean region, *Geophys. J. Int.*, *159*, 275–290, doi:10.1111/j.1365-246X.2004.02381.x.
- Schmid, C., S. Van der Lee, J. C. VanDecar, E. R. Engdahl, and D. Giardini (2008), Three-dimensional S velocity of the mantle in the Africa-Eurasia plate boundary region from phase arrival times and regional waveforms, *J. Geophys. Res.*, *113*, B03306, doi:10.1029/2005JB004193.
- Selvaggi, G., and A. Amato (1992), Subcrustal earthquakes in the northern Apennines (Italy): Evidence for a still active subduction? *Geophys. Res. Lett.*, *19*, 2127–2130, doi:10.1029/92GL02503.
- Serri, G., F. Innocenti, and P. Manetti (1993), Geochemical and petrological evidence of the subduction of delaminated Adriatic continental lithosphere in the genesis of the Neogene-Quaternary magmatism of central Italy, *Tectonophysics*, *223*, 117–147, doi:10.1016/0040-1951(93)90161-C.
- Sieminski, A., J.-J. Lévesque, and E. Debayle (2004), Can finite-frequency effects be accounted for in ray theory surface wave tomography? *Geophys. Res. Lett.*, *31*, L24614, doi:10.1029/2004GL021402.
- Sleep, N. H. (1990), Hot spots and mantle plumes: Some phenomenology, *J. Geophys. Res.*, *95*, 6715–6736, doi:10.1029/JB095iB05p06715.
- Smyth, J. R. (1987), β -Mg₂SiO₄: A potential host for water in the mantle? *Am. Mineral.*, *72*, 1051–1055.
- Soudoufi, F. (2005), Lithospheric structure of the Aegean obtained from P and S receiver functions, Ph.D. thesis, Free Univ. of Berlin, Berlin.
- Spakman, W., M. J. R. Wortel, and N. J. Vlaar (1988), The Hellenic subduction zone: A tomographic image and its geodynamic implications, *Geophys. Res. Lett.*, *15*, 60–63, doi:10.1029/GL015i001p00060.
- Spakman, W., S. Van der Lee, and R. Van der Hilst (1993), Travel-time tomography of the European-Mediterranean mantle down to 1400 km, *Phys. Earth Planet. Inter.*, *79*, 3–74, doi:10.1016/0031-9201(93)90142-V.
- Stampfli, G. M., and G. D. Borel (2002), A plate tectonic model for the Paleozoic and Mesozoic constrained by dynamic plate boundaries and restored synthetic oceanic isochrones, *Earth Planet. Sci. Lett.*, *196*, 17–33, doi:10.1016/S0012-821X(01)00588-X.
- Tatar, M., D. Hatzfeld, and M. Ghafory-Ashitiani (2004), Tectonics of the Central Zagros (Iran) deduced from microearthquake seismicity, *Geophys. J. Int.*, *156*, 255–266, doi:10.1111/j.1365-246X.2003.02145.x.
- Tesauro, M., M. K. Kaban, and S. A. P. L. Cloetingh (2008), EuCRUST-07: A new reference model for the European crust, *Geophys. Res. Lett.*, *35*, L05313, doi:10.1029/2007GL032244.
- Tkalčić, H., M. E. Pasyanos, A. J. Rodgers, R. Gok, W. R. Walter, and A. Al-Amri (2006), A multistep approach for joint modeling of surface wave dispersion and teleseismic receiver functions: Implications for lithospheric structure of the Arabian Peninsula, *J. Geophys. Res.*, *111*, B11311, doi:10.1029/2005JB004130.
- VanDecar, J. C. (1991), Upper-mantle structure of the Cascadia subduction zone from non-linear teleseismic travel-time inversion, Ph.D. thesis, Univ. of Wash., Seattle.
- VanDecar, J. C., and R. S. Crosson (1990), Determination of teleseismic relative phase arrival times using multi-channel cross-correlation and least-squares, *Bull. Seismol. Soc. Am.*, *80*, 150–169.
- van der Lee, S., and G. Nolet (1997), Upper mantle S velocity structure of North America, *J. Geophys. Res.*, *102*, 22,815–22,838, doi:10.1029/97JB01168.
- van der Lee, S., and A. Frederiksen (2005), Surface wave tomography applied to the North American upper mantle, in *Seismic Earth: Array Analysis of Broadband Seismograms*, *Geophys. Monogr. Ser.*, vol. 157, edited by A. Levander and G. Nolet, pp. 67–80, AGU, Washington, D. C.
- van der Lee, S., et al. (2001), Eurasia-Africa plate boundary region yields new seismographic data, *Eos Trans. AGU*, *82*, 637–646, doi:10.1029/01EO00367.
- van der Lee, S., K. Regenauer-Lieb, and D. A. Yuen (2008), The role of water in connecting past and future episodes of subduction, *Earth Planet. Sci. Lett.*, *273*, 15–27, doi:10.1016/j.epsl.2008.04.041.
- van der Meulen, M. J., J. E. Meulenkamp, and M. J. R. Wortel (1998), Lateral shifts of Apenninic foredeep depocentres reflecting detachment of subducted lithosphere, *Earth Planet. Sci. Lett.*, *154*, 203–219, doi:10.1016/S0012-821X(97)00166-0.
- van der Meulen, M. J., T. J. Kouwenhoven, G. J. van der Zwaan, J. E. Meulenkamp, and M. J. R. Wortel (1999), Late Miocene uplift in the Romagnan Apennines and the detachment of subducted lithosphere, *Tectonophysics*, *315*, 319–335, doi:10.1016/S0040-1951(99)00282-6.
- Van der Voo, R., W. Spakman, and H. Bijwaard (1999), Tethyan subducted slabs under India, *Earth Planet. Sci. Lett.*, *171*, 7–20, doi:10.1016/S0012-821X(99)00131-4.
- Villaseñor, A., M. H. Ritzwoller, A. L. Levshin, M. P. Barmin, E. R. Engdahl, W. Spakman, and J. Trampert (2001), Shear velocity structure of central Eurasia from inversion of surface wave velocities, *Phys. Earth Planet. Inter.*, *123*, 169–184, doi:10.1016/S0031-9201(00)00208-9.
- Walker, R. T., P. Gans, M. B. Allen, J. Jackson, M. Khatib, N. Marsh, and M. Zarrinkoub (2009), Late Cenozoic volcanism and rates of active faulting in eastern Iran, *Geophys. J. Int.*, *177*, 783–805, doi:10.1111/j.1365-246X.2008.04024.x.
- Wessel, P., and W. H. F. Smith (1998), New, improved version of the Generic Mapping Tools released, *Eos Trans. AGU*, *79*, 579, doi:10.1029/98EO00426.
- Wilde-Piórko, M., J. Saul, and M. Grad (2005), Differences in the crustal and uppermost mantle structure of the Bohemian massif from teleseismic receiver functions, *Stud. Geophys. Geod.*, *49*, 85–107, doi:10.1007/s11200-005-1627-3.
- Wortel, M. J. R., and W. Spakman (2000), Subduction and slab detachment in the Mediterranean-Carpathian region, *Science*, *290*, 1910–1917, doi:10.1126/science.290.5498.1910.
- Yang, Y., M. H. Ritzwoller, A. L. Levshin, and N. M. Shapiro (2007), Ambient noise Rayleigh wave tomography across Europe, *Geophys. J. Int.*, *168*, 259–274, doi:10.1111/j.1365-246X.2006.03203.x.
- Yoshizawa, K., and B. L. N. Kennett (2005), Sensitivity kernels for finite-frequency surface waves, *Geophys. J. Int.*, *162*, 910–926, doi:10.1111/j.1365-246X.2005.02707.x.
- Zeyen, H., F. Volker, V. Wehrle, K. Fuchs, S. V. Sobolev, and R. Altherr (1997), Styles of continental rifting: Crust-mantle detachment and mantle plumes, *Tectonophysics*, *278*, 329–352, doi:10.1016/S0040-1951(97)00111-X.
- Zhou, Y., G. Nolet, F. A. Dahlen, and G. Laske (2006), Global upper-mantle structure from finite-frequency surface-wave tomography, *J. Geophys. Res.*, *111*, B04304, doi:10.1029/2005JB003677.
- Zielhuis, A., and G. Nolet (1994), Shear-wave velocity variations in the upper mantle beneath central Europe, *Geophys. J. Int.*, *117*, 695–715, doi:10.1111/j.1365-246X.1994.tb02463.x.
- Zor, E., E. Sandvol, C. Gürbüz, N. Türkelli, D. Seber, and M. Barazangi (2003), The crustal structure of the East Anatolian plateau (Turkey) from receiver functions, *Geophys. Res. Lett.*, *30*(24), 8044, doi:10.1029/2003GL018192.

H. Bedle, Chevron North America Exploration and Production Company, Gulf of Mexico SBU, 100 Northpark Blvd., Covington, LA 70433, USA.

S.-J. Chang and S. van der Lee, Department of Earth and Planetary Sciences, Northwestern University, 1850 Campus Dr., Evanston, IL 60208-2150, USA. (suzan@earth.northwestern.edu)

M. P. Flanagan, E. M. Matzel, M. E. Pasyanos, and A. J. Rodgers, Lawrence Livermore National Laboratory, PO Box 808, L-205, Livermore, CA 94551, USA.

F. Marone, Swiss Light Source, Paul Scherrer Institut, CH-5232 Villigen, Switzerland.

B. Romanowicz, Berkeley Seismological Lab., University of California, Berkeley, CA, USA.

C. Schmid, Schweizerische Mobiliar Versicherungsgesellschaft, Bundesgasse 35, Postfach, CH-3001 Bern, Switzerland.